
Crustal and Upper Mantle Structures Beneath the Arabian Shield and Red Sea

Abdullah Al Amri, K. Abdelrahman, M.O. Andreae, and M. Al-Dabbagh

Abstract

The Arabian Shield and Red Sea region is considered one of only a few places in the world undergoing active continental rifting and formation of new oceanic lithosphere. We determined the seismic velocity structure of the crust and upper mantle beneath this region using broadband seismic waveform data. We estimated teleseismic receiver functions from high-quality waveform data. The raw data for RF analysis consist of 3-component broadband velocity seismograms for earthquakes with magnitudes $M_w > 5.8$ and epicentral distances between 30° and 90° . We performed several state-of-the-art seismic analyses of the KACST and SGS data. Teleseismic P- and S-wave travel time tomography provides an image of upper mantle compressional and shear velocities related to thermal variations. We present a multi-step procedure for jointly fitting surface-wave group-velocity dispersion curves (from 7 to 100 s for Rayleigh and 20 to 70 s for Love waves) and teleseismic receiver functions for lithospheric velocity structure. The method relies on an initial grid search for a simple crustal structure, followed by a formal iterative inversion, an additional grid search for shear wave velocity in the mantle and finally forward modeling of transverse isotropy to resolve surface-wave dispersion discrepancy. Inversions of receiver functions have poor sensitivity to absolute velocities. To overcome this shortcoming we have applied the method of Julia et al. (Geophys J Int 143:99–112, 2000), which combines surface-wave group velocities with receiver functions in formal inversions for crustal and uppermost mantle velocities. The resulting velocity models provide new constraints on crustal and upper mantle structure in the Arabian Peninsula. While crustal thickness and average crustal velocities are consistent with many previous studies, the results for detailed mantle structure are completely new. Finally, teleseismic shear-wave splitting was measured to estimate upper mantle anisotropy. These analyses indicate that stations near the Gulf of Aqabah display fast orientations that are aligned parallel to the Dead Sea Transform Fault, most likely related to the strike-slip motion between Africa and Arabia. The remaining stations across Saudi Arabia yield statistically the same result, showing a consistent pattern of north-south oriented fast directions with delay times averaging about 1.4 s. The uniform anisotropic signature across Saudi Arabia is best explained by a combination of plate and density driven flow in the asthenosphere. By combining the northeast oriented flow associated with absolute plate motion with the northwest oriented flow associated with the channelized Afar plume along the Red Sea, we

A. Al Amri (✉) · K. Abdelrahman · M.O. Andreae ·
M. Al-Dabbagh
Geology and Geophysics Department, King Saud University,
Riyadh, Saudi Arabia
e-mail: alamri.geo@gmail.com

M.O. Andreae
Biogeochemistry Department, Max Planck Institute for Chemistry,
Mainz, Germany

obtain a north-south oriented resultant that matches our splitting observations and supports models of the active rifting processes. This explains why the north-south orientation of the fast polarization direction is so pervasive across the vast Arabian Plate. Seafloor spreading in the Red Sea is non-uniform, ranging from nearly 0.8 cm/a in the north to about 2 cm/a in the south. The Moho and LAB are shallowest near the Red Sea and become deeper towards the Arabian interior. Near the coast, the Moho is at a depth of about 22–25 km. Crustal thickening continues until an average Moho depth of about 35–40 km is reached beneath the interior Arabian Shield. The LAB near the coast is at a depth of about 55 km; however, it also deepens beneath the Shield to attain a maximum depth of 100–110 km. At the Shield-Platform boundary, a step is observed in the lithospheric thickness where the LAB depth increases to about 160 km. This study supports multi plume model, which states that there are two separated plumes beneath the Arabian Shield, and that the lower velocity zones (higher temperature zones) are related to volcanic activities and topographic characteristics on the surface of the Arabian Shield. In addition, our results suggest a two-stage rifting history, where extension and erosion by flow in the underlying asthenosphere are responsible for variations in LAB depth. LAB topography guides asthenospheric flow beneath western Arabia and the Red Sea, demonstrating the important role lithospheric variations play in the thermal modification of tectonic environments.

Keywords

Crustal • Upper mantle • Structures • Arabian Shield • Red Sea

Introduction

The Arabian Peninsula presents several interesting seismological problems. On the west, rifting in the Red Sea has split a large Precambrian Shield. Active rifting is responsible for the geometry of the plate margins in the west and southwest. To the south, similar rifting running in a more east-west direction through the Gulf of Aden has separated the Arabian Peninsula from Africa. In the northwest, the Gulf of Aqabah forms the southernmost continuation of the Dead Sea transform. The northern and northeastern boundaries of the Arabian Plate are areas of continental collision, with the Arabian Plate colliding with the Persian Plate.

King Saud University (KSU) and King Abdulaziz City for Science and Technology (KACST) operate the seismic networks in Saudi Arabia since 1985 (Al-Amri and Al-Amri 1999a, b). Both networks feature the Boulder Real Time Technologies (BRTT) Antelope system, however the networks operate independently. Data is collected and transmitted in real time to the central processing facilities in Riyadh. Events are automatically detected and located and waveforms are excerpted for later analysis, while continuous data are archived. The KACST network features 37 stations (26 BB STS-2 and 11 SP sensors). The system uses the IASP91 earth model to locate events. Figure 1 shows all events with magnitude greater than 5.5 recorded by the KACST stations between 2000 and 2004. Events we had access to are shown in red. The large number of new events in the proper distance range for S and SKS splitting analysis

are sufficient to allow us to investigate patterns of splitting parameters with arrival direction and determine whether more complex anisotropic models are required below the Red Sea Rift. In 2005, The Saudi Geological Survey (SGS) began operating the national seismographic network in Jeddah, Saudi Arabia. Recently, it consists of more than 120 broadband stations (Nanometrics Trillium broadband seismometers, 24-bit digitizers, GPS receivers, and VSAT transceivers) distributed across the Arabian Shield.

The Saudi Arabian Broadband Deployment (SABD, Vernon et al. 1996) provided the first data set of broadband recordings in this region. This deployment consisted of 9 broadband three-component seismic stations along a similar transect to an early seismic refraction study (Mooney et al. 1985; Gettings et al. 1986; Mechie et al. 1986). Data from the experiment resulted in several studies and models of the seismic structure of the Arabian Shield (Sandvol et al. 1998a, b; Mellors et al. 1999; Rodgers et al. 1999; Benoit et al. 2003; Al-Amri et al. 2004; Al-Damegh et al. 2004). These studies provided new constraints on crustal and upper mantle structure. The crustal model of the western Arabian Platform shows a little higher P-velocity for the upper crust in the Shield than in the Platform and the crustal Platform seems to have a greater thickness than the Shield by about 3 km. The Moho discontinuity beneath the western Arabian Platform indicates a velocity of 8.2 km/s of the upper mantle and a 42 km MOHO depth (Al-Amri 1998a, b, 1999a, b).

Generally, the crustal thickness in the Arabian Shield area varies from 35 to 40 km in the west adjacent to the Red Sea

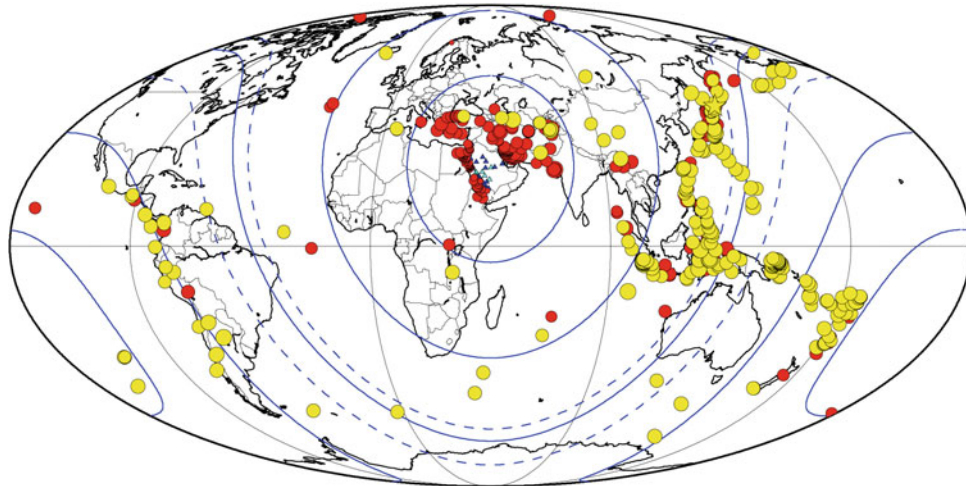
Teleseismic events with $M > 5.5$ between 2000-2004

Fig. 1 Map of the world centered on the Red Sea showing events recorded by KACST and SGS broadband stations between 2000 and 2001 (*red*) and 2002–2004 (*yellow*). Events outside the first contour (30°) are at teleseismic distances and all have magnitude >5.5 . Some

events within the 30° contour have magnitudes <5.5 . Many of the *red* events (2000–2001) in the western Pacific subduction zones are hidden beneath the more recent events (*yellow*)

to 45 km in central Arabia (Sandvol et al. 1998a, b; Rodgers et al. 1999). Not surprising the crust thins nears the Red Sea (Mooney et al. 1985; Gettings et al. 1986; Mechie et al. 1986). High-frequency regional S-wave phases are quite different for paths sampling the Arabian Shield than those sampling the Arabian Platform (Mellors et al. 1999; Sandvol et al. 1998a, b). In particular the mantle Sn phase is nearly absent for paths crossing parts of the Arabian Shield, while the crustal Lg phase is of extremely large amplitude. This may result from an elastic propagation effect or extremely high mantle attenuation and low crustal attenuation occurring simultaneously, or a combination of both.

The Red Sea is a region of current tectonic activity where continental lithosphere is being ruptured to form oceanic lithosphere, as the opening of the Red Sea split the Arabian-Nubian Shield. While much work has been done to understand the uplift and volcanism of the Arabian Shield, little is known about the structure of the underlying upper mantle. The Arabian Shield consists of at least five Precambrian terranes separated by suture zones (Schmidt et al. 1979). During the late Oligocene and early Miocene, the Arabian Shield was disrupted by the development of the Red Sea and Gulf of Aden rifts, and from the mid-Miocene to the present, the region experienced volcanism and uplift (Bohannon et al. 1989). The uplift and volcanism are generally assumed to be the result of hot, buoyant material in the upper mantle that may have eroded the base of the lithosphere (Camp and Roobol 1992). However, details about the nature of the upper mantle, such as its thermal and compositional state, are not known.

Saudi Arabia and the Red Sea Rift zone offer an excellent environment in which to study the seismic anisotropy

associated with rifting and extension. Several different types of models have been proposed to explain how continental rifting in the Red Sea developed. The passive rifting model assumes simple shear conditions, where extensional stresses are accommodated on large-scale detachment planes extending through the entire lithosphere below the rift. Flow beneath the rift is parallel to the direction of extension as the underlying asthenosphere is passively upwelled, which would predict a rift-perpendicular ϕ . The active rifting model involves thinning of the lithosphere by flow in the underlying asthenosphere and requires the presence of hot, ascending material (Camp and Roobol 1992; Ebinger and Sleep 1998; Daradich et al. 2003). In this case, local convection may lead to more complicated flow patterns and therefore more complex anisotropy at depth. Several studies have suggested that these two end-member models may not be mutually exclusive; rifting in the Red Sea may have been initiated by far-field collision and passive processes, followed by more recent active processes associated with a mantle plume (Camp and Roobol 1992; Ebinger and Sleep 1998; Daradich et al. 2003).

Several previous studies have examined the anisotropic characteristics in the vicinity of the Red Sea Rift and show a fairly consistent pattern. Using eight PASSCAL stations across the Arabian Shield, Wolfe et al. (1999) performed shear-wave splitting analysis and found δt of 1.0–1.5 s and ϕ oriented approximately north-south. Using receiver functions, Levin and Park (2000) found evidence for a more complex anisotropic structure beneath the PASSCAL station RAYN consisting of two dipping layers at depth, but again with a resultant ϕ oriented north-south. Further north, Schmid et al. (2004) and Levin et al. (2006) examined splitting

at several stations near the Gulf of Aqabah and the Dead Sea Transform Fault, where they found average δt of about 1.3 s and ϕ slightly east of north, with some evidence for a more complex, two-layer anisotropic model. However, each of these studies was somewhat limited in their station distribution and data availability. Hansen et al. (2006) presented a more comprehensive analysis of the anisotropic signature along the Red Sea and across Saudi Arabia by analyzing shear-wave splitting recorded by stations from three different seismic networks. This is the largest, most widely distributed array of stations examined across Saudi Arabia to date. They demonstrated that the north-south orientation of the fast polarization direction is not just valid at isolated sites on the Arabian Shield, but extends throughout the whole of Arabia.

In this paper, we extend previous efforts to determine crustal and lithospheric mantle structure under the Arabian Shield and Red Sea by applying an improved method for inverting receiver functions and shear wave group velocity (SWGVS) measurements. We apply this technique to a number of stations that sample the complexity of tectonic environments and provide new constraints on structure.

While there have been many studies of this topic using a wide variety of techniques, many questions about the structure of the Arabian Peninsula remain unanswered. A thorough understanding of the seismic structure and wave propagation characteristics of the region must be established before we can proceed to assess seismic hazard. We implemented several types of analysis to seismic data recorded by KACST and SGS seismic networks. These analyses include:

- teleseismic P- and S-wave travel time tomography;
- teleseismic receiver functions for crustal structure;
- teleseismic receiver functions for upper mantle discontinuity structure;
- teleseismic shear-wave splitting; and
- regional and far-regional surface waveform modeling.

Together these analyses result in a unified model of the structure and physical state of the lithosphere beneath the Arabian Shield and Red Sea. The dense station spacing and excellent quality of the KACST and SGS data allow for very detailed resolution of the structures.

Seismotectonics and Seismic Structures

The Arabian Peninsula consists of a single tectonic plate, the Arabian Plate. It is surrounded on all sides by active plate boundaries as evidenced by earthquake locations. Figure 2 shows a map of the Arabian Peninsula along with major tectonic features and earthquake locations. The active tectonics of the region is dominated by the collision of the Arabian Plate with the Eurasian Plate along the Zagros and

Bitlis Thrust systems, rifting and seafloor spreading in the Red Sea and Gulf of Aden. Strike-slip faulting occurs along the Gulf of Aqabah and Dead Sea Transform fault systems. The great number of earthquakes in the Gulf of Aqabah poses a significant seismic hazard to Saudi Arabia. Large earthquakes in the Zagros Mountains of southern Iran may lead to long-period ground motion in eastern Saudi Arabia.

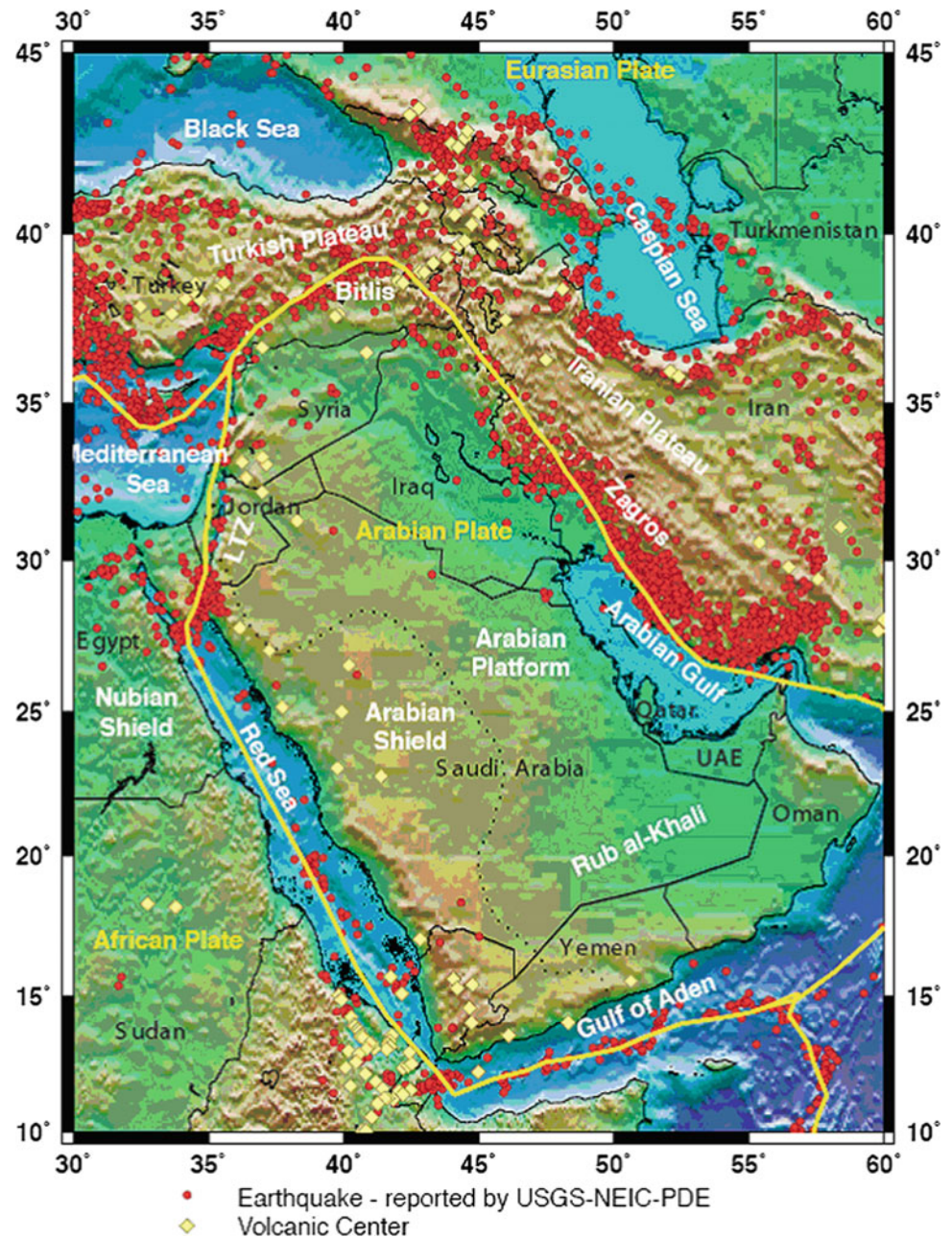
The two large regions, associated with the presence or absence of sedimentary cover, define the large-scale geologic structure of the Arabian Peninsula. The Arabian Platform (eastern Arabia) is covered by sediments that thicken toward the Arabian Gulf. In contrast, the Arabian Shield has no appreciable sedimentary cover, with many outcrops of bedrock. Figure 3 shows the sediment thickness, estimated from compiled drill hole, gravity, and seismic reflection data (Seber et al. 1997). The Arabian Shield consists of at least five Precambrian terranes separated by suture zones (Schmidt et al. 1979). During the late Oligocene and early Miocene, the Arabian Shield was disrupted by the development of the Red Sea and Gulf of Aden rifts, and from the mid-Miocene to the present, the region experienced volcanism and uplift (Bohannon et al. 1989). The uplift and volcanism are generally assumed to be the result of hot, buoyant material in the upper mantle that may have eroded the base of the lithosphere (Camp and Roobol 1992). However details about the nature of the upper mantle, such as its thermal and compositional state, are not known. Volcanic activity (the Harrats) is observed on the Arabian Shield (Fig. 2). This is likely related to the opening of the Red Sea and mantle asthenospheric upwelling beneath western Arabia (e.g. Camp and Roobol 1992).

The northwestern regions of Saudi Arabia are distinct from the Arabian Shield, as this region is characterized by high seismicity in the Gulf of Aqabah and Dead Sea Rift. Active tectonics in this region is associated with the opening of the northern Red Sea and Gulf of Aqabah, as well as a major continental strike-slip plate boundary.

The Dead Sea transform system connects active spreading centers of the Red Sea to the area where the Arabian Plate is converging with Eurasia in southern Turkey. The Gulf of Aqabah in the southern portion of the rift system has experienced left-lateral strike-slip faulting with a 110 km offset since the early Tertiary to the present. The seismicity of the Dead Sea transform is characterized by both swarm and mainshock-aftershock types of earthquake activities. The instrumental and historical seismic records indicate a seismic slip rate of 0.15–0.35 cm/year during the last 1000–1500 years, while estimates of the average Pliocene-Pleistocene rate are 0.7–1.0 cm/year.

Historically, the most significant earthquakes to hit the Dead Sea region were the events of 1759 (Damascus), 1822 (Aleppo), and of 1837; 1068 (Gulf of Aqabah area) caused deaths of more than 30,000 people. Ben Menahem (1979) indicated that about 26 major earthquakes ($6.1 < ML < 7.3$)

Fig. 2 Map of the Arabian Peninsula and surrounding regions. Major geographic and tectonic/geologic features are indicated. Plate boundaries are indicated by *yellow lines*. Earthquakes and volcanic centers are shown as *red circles* and *yellow diamond*, respectively



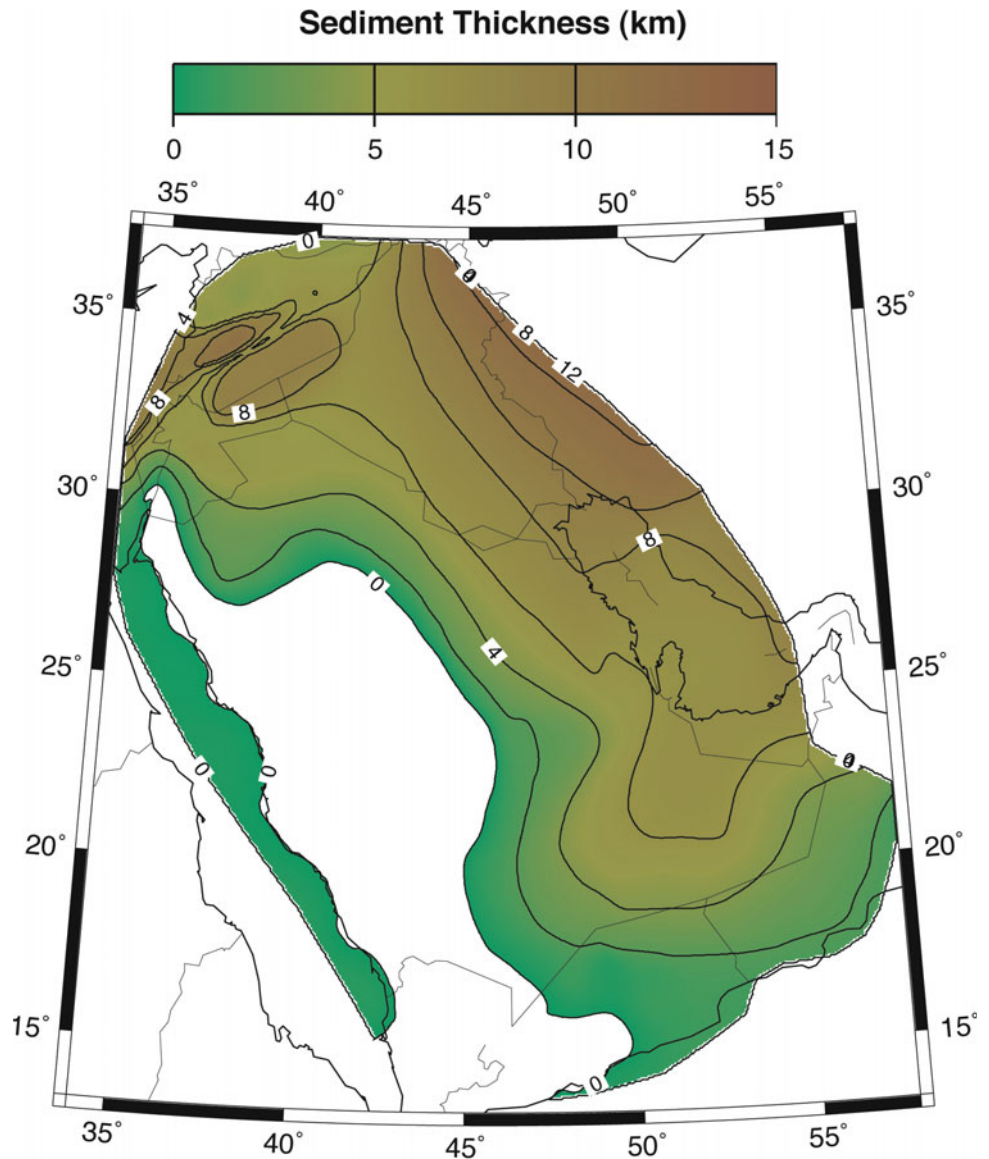
occurred in southern Dead Sea region between 2100 B.C. and 1900 A.D. In 1980 and 1990, the occurrence of earthquake swarms in 1983, 1985, 1991, 1993 and 1995 in the Gulf of Aqabah clearly indicates that this segment is one of the most seismically active zones in the Dead Sea transform system. Earthquake locations provide evidence for continuation of the faulting regime from the Gulf northeastward inland beneath thick sediments, suggesting that the northern portion of the Gulf is subjected to more severe seismic hazard compared to the southern portion (Al-Amri et al. 1991).

To the south, the majority of earthquakes and tectonic activity in the Red Sea region are concentrated along a belt

that extends from the central Red Sea region south to Afar and then east through the Gulf of Aden. There is little seismic activity in the northern part of the Red Sea, and only three earthquakes have been recorded north of latitude 25°N. Instrumental seismicity of the northern Red Sea shows that 68 earthquakes ($3.8 < m_b < 6.0$) are reported to have occurred in the period from 1964 to 1993.

Historically, about 10 earthquakes have occurred during the period 1913–1994 with surface-wave (M_s) magnitudes between 5.2 and 6.1. Some of these events were associated with earthquake swarms, long sequences of shocks and aftershocks (the earthquakes of 1941, 1955, 1967 and 1993).

Fig. 3 Sediment thickness of the Arabian Plate, estimated from compiled drill hole, gravity, and seismic reflection data



The occurrence of the January 11, 1941 earthquake in the northwest of Yemen ($M_s = 5.9$) with an aftershock on February 4, 1941 ($M_s = 5.2$), the earthquake of October 17, 1955 ($M_s = 4.8$), and the 1982 Yemen earthquake of magnitude 6.0 highlight the hazards that may result from nearby seismic sources and demonstrate the vulnerability of northern Yemen to moderate-magnitude and larger earthquakes. Instrumental seismicity of the southern Red Sea shows that 170 earthquakes ($3.0 < m_b < 6.6$) are reported to have occurred in the period 1965–1994. The historical and instrumental records of strong shaking in the southern Arabian Shield and Yemen (1832; 1845; 1941; 1982 and 1991) indicate that the return period of severe earthquakes that affect the area is about 60 years (Al-Amri 1995).

The Arabian Plate boundary extends east-northeast from the Afar region through the Gulf of Aden and into the Arabian

Sea and Zagros fold belt. The boundary is clearly delineated by teleseismic epicenters, although there are fewer epicenters bounding the eastern third of the Arabian Plate south of Oman. Most seismicity occurs in the crustal part of the Arabian Plate beneath the Zagros folded belt (Jackson and Fitch 1981). The Zagros is a prolific source of large magnitude earthquakes with numerous magnitude 7+ events occurring in the last few decades. The overall lack of seismicity in the interior of the Arabian Peninsula suggests that little internal deformation of the Arabian Plate is presently occurring.

Seismic structure studies of the Arabian Peninsula have been varied, with dense coverage along the 1978 refraction survey and little or no coverage of the aseismic regions, such as the Empty Quarter. In 1978, the Directorate General of Mineral Resources of Saudi Arabia and the U.S. Geologic Survey conducted a seismic refraction survey aimed at

determining the structure of the crust and upper mantle. This survey was conducted primarily in the Arabian Shield along a line from the Red Sea to Riyadh. Reports of crust structure found a relatively fast-velocity crust with thickness of 38–43 km (Mooney et al. 1985; Mechie et al. 1986; Gettings et al. 1986, Badri 1991). The crust in the western shield is slightly thinner than that in the eastern shield. Mooney et al. (1985) suggested that the geology and velocity structure of the Shield can be explained by a model in which the Shield developed in the Precambrian by suturing of island arcs. They interpret the boundary between the eastern shield and the Arabian Platform as a suture zone between crustal blocks of differing composition.

Surface waves observed at the long-period analog stations RYD (Riyadh), SHI (Shiraz, Iran), TAB (Tabriz, Iran), HLW (Helwan, Egypt), AAE (Addis-Ababa, Ethiopia) and JER (Jerusalem) were used to estimate crustal and upper mantle structure (Seber and Mitchell 1992; Mokhtar and Al-Saeed 1994). These studies reported faster crustal velocities for the Arabian Shield and slower velocities for the Arabian Platform. The Saudi Arabian Broadband Deployment (Vernon and Berger 1997; Al-Amri et al. 1999) provided the first data set of broadband recordings from this region. This deployment consisted of 9 broadband three-component seismic stations along a similar transect to an early seismic refraction study (Mooney et al. 1985; Gettings et al. 1986; Mechie et al. 1986). Data from the experiment resulted in several studies and models (Sandvol et al. 1998a, b; Mellors et al. 1999; Rodgers et al. 1999; Benoit et al. 2003). These studies provided new constraints on crustal and upper mantle structure. The crustal model of the western Arabian Platform shows a little higher P-velocity for the upper crust in the Shield than in the Platform, and the crustal Platform seems to have a greater thickness than in the Shield by about 3 km. The Moho discontinuity beneath the western Arabian Platform indicates a velocity of 8.2 km/s of the upper mantle and a 42 km Moho depth (Al-Amri 1998a, b, 1999a, b). Julià et al. (2003) presented velocity models for the same stations, combining RF with surface wave dispersion data to invert for structure. Al-Damegh et al. (2005) calculated RF's for the Arabian Plate from permanent broadband stations in Saudi Arabia (Al-Amri and Al-Amri 1999a, b) and Jordan (Rodgers et al. 2003).

Methodology

We improved our understanding of the crustal structures and upper mantle of the Red Sea and the Arabian Shield by using broadband waveform data from the KACST, RAYN/GSN (Fig. 4) and SGS Digital Seismic Networks. This paper includes standard seismological investigations as well as newly developed techniques as follows:

Data Collection and Validation

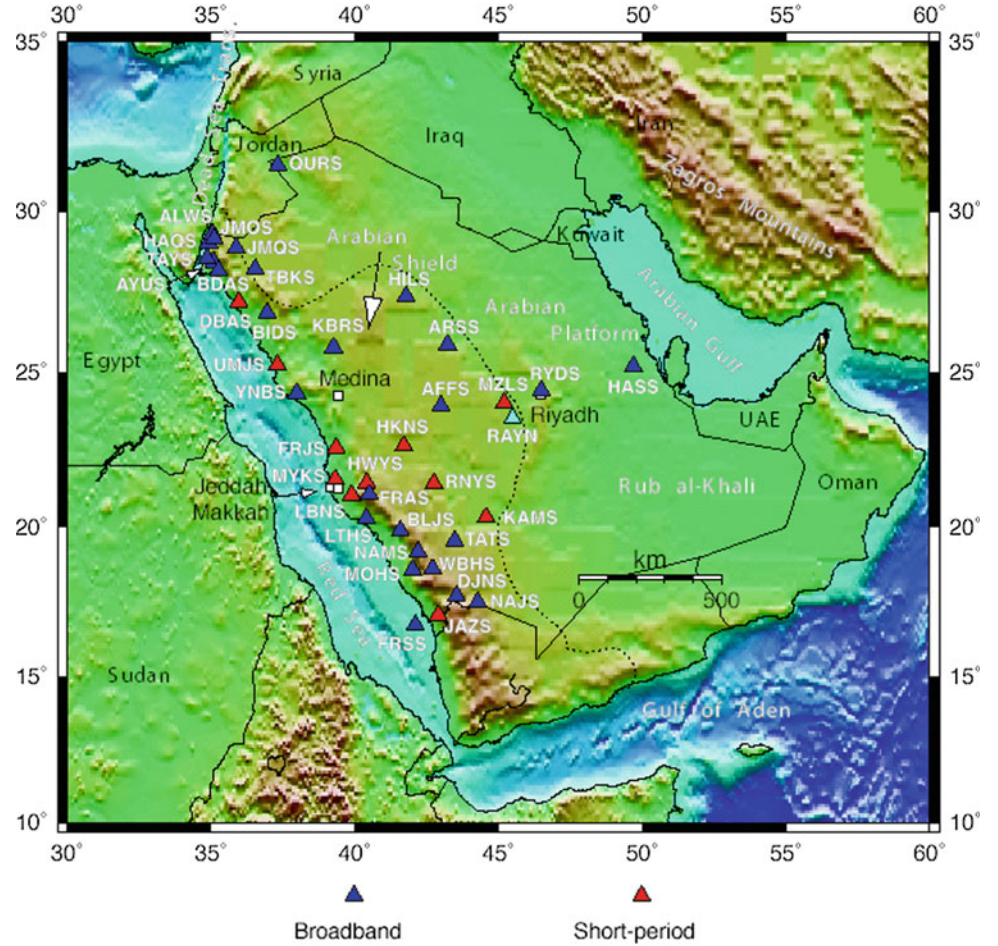
The investigators wrote software to extract waveform data. This software facilitated the extraction and exchange of seismic waveform and parameter data. In order to validate the station timing and instrument response we performed comparisons of timing and amplitudes of P-waves for large teleseismic events at the KACST and SGS stations with the Global Seismic Station RAYN. This station has well calibrated timing and instrument response. The relative arrival times of teleseismic P-waves at the KACST stations can be accurately measured by cross-correlating with the observed waveforms at RAYN and correcting for distance effects. Absolute amplitudes of teleseismic P-waves at the KACST, SGS and RAYN stations were measured by removing the instrument response, gain, and band-pass filtering.

This study also considered many events and computed average travel time and amplitude residuals relative to a globally averaged one dimensional earth model, such as IASP91. Although there were deviations between the timing and amplitudes of the KACST and SGS P-waves from the predictions of the iasp91 model (because of lateral heterogeneity), the tests were useful to identify which stations might have timing and/or instrument calibration problems.

Teleseismic Travel Time Tomography

A number of tomographic methods are available for using P- and S-wave travel time delays to image upper mantle velocity variations (e.g., Thurber 1983; VanDecar 1991; Evans and Achauer 1993). We used these methods to image relative velocity variations in the upper mantle beneath the Arabian Shield. An example of the results we obtained is provided by a recent study by Benoit et al. (2003) of upper mantle P-wave velocity structure under the Arabian Shield. In this study, P-wave travel time residuals were determined from the SABD dataset using the multi-channel cross correlation (MCCC) method of VanDecar and Crossen (1990) and then modeled using the inversion method of VanDecar (1991). The MCCC method of VanDecar and Crossen (1990), which makes use of the waveform coherency that is found across a regional network, involves three steps. First, the data is band-passed filtered between 0.5 and 5 Hz. A cross correlation is then computed for all possible pairs of stations to find the relative arrival times, and finally a least squares optimization scheme is applied to the arrival times to minimize inconsistencies in the data. The uncertainties in the relative P-wave travel times obtained from the SABD dataset are about 0.1 to 0.15 s. After computing the travel time residuals, they were inverted for P-wave slowness and earthquake relocations. The inversion searches for the smoothest model with the least amount of structure that will

Fig. 4 Map of the stations from the KACST digital seismic network and RAYN/GSN



match the data. The inversion is linear and minimizes both spatial gradients and model roughness using a conjugate gradient scheme. Root mean square (rms) and variance reduction (VR) for each model are calculated as a measure of misfit according to the following expressions:

$$rms = \sqrt{\frac{N_{max}}{N}} \sqrt{\frac{\sum_{i=1}^N w_i (obs_i - theor_i)^2}{N}};$$

$$VR = \left\{ 1 - \frac{\sum_i (obs_i - theor_i)^2}{\sum_i obs_i^2} \right\} 100\%$$

where N is the number of selected periods for Love or Rayleigh wave dispersion at a given station (typically, we consider 11 discrete periods spanning from 20 to 70 s for Love waves, and 20 discrete periods spanning from 7 to 100 s for Rayleigh waves), and N_{max} is the number of periods for Rayleigh wave dispersion. The factor $\sqrt{\frac{N_{max}}{N}}$ is then a normalization factor, which equalizes the relative

significance of rms results for Love and Rayleigh wave dispersion, given the fact that less data points are available for Love waves. The parameter w_i is defined as $1/e$ (where e is the error of each point in surface wave dispersion curves) and is a relative weight of each velocity measurement in the dispersion. If there is a large misfit at only period of the group velocity dispersion, the above expression for rms would significantly impact the result. However, the above expression for variance reduction would not significantly penalize the result. Therefore, variance reduction is a more appropriate measure of misfit than rms for waveforms (receiver functions) with a much larger number of points than in discrete dispersion measurements, where it is important to fit the character of the waveform. The rms and VR expressions are used in combination as criteria for selecting and plotting small percentages of the best models.

Overall, even though the resulting models consisting of a 3-layer crust and a half space are in many cases too simplistic, we note that some excellent matches of the data by the synthetics were found, particularly in cases when only receiver function or only surface wave data (either Love or Rayleigh wave dispersion) are considered.

Receiver Functions

The use of P-wave receiver functions to infer the existence of major crustal and upper mantle discontinuities has become a standard technique in seismology. These methods are described elsewhere (e.g., Langston 1979; Owens et al. 1984; Ammon 1991) and consist of deconvolving the vertical P-wave component from the radial (and possibly tangential) component to expose P-to-S converted waves in the P-wave coda. The timing and amplitude of these conversions are then modeled or incorporated in inversion algorithms to infer S-wave velocity models and the depth to the discontinuities. We performed P-wave receiver function studies for some stations of the network. To image crustal structure, we combined the receiver functions with surface wave dispersion measurements out to 30 s using the joint receiver function/surface wave inversion method of Julia et al. (2000). This method, then, provides a simple way to control trade-offs between fitting the receiver functions and the dispersion curves (normalized by the data uncertainty and number of points), and also the trade-off between fitting the data and model smoothness. Both smoothness and weighting parameters are estimated empirically, after running a suite of inversions.

The combination of receiver functions with surface wave dispersion measurements allowed us to place tight constraints on average crustal S velocities and Moho depths.

Teleseismic Shear Wave Splitting

The most abundant and highly anisotropic upper mantle mineral, olivine, develops preferred lattice orientations when deformed in the dislocation creep regime (Karato 1998). For large strains, the olivine axes become parallel to the direction of shear. Therefore, measurements of seismic anisotropy can be used to investigate mantle deformation. While seismic anisotropy has been studied in several diverse tectonic settings, its interpretation in many cases is still enigmatic. No tectonic environment has been more difficult to understand than rift zones. Since Hess' (1964) pioneering study of anisotropy in ocean basins, it has been expected that extension should align fast directions of olivine parallel to the rifting direction through shear in the lithosphere or asthenosphere. However, recent studies of seismic anisotropy from SKS splitting in the Basin and Range (Savage et al. 1990), the Rio Grande Rift (Sandvol et al. 1992), the Baikal Rift (Gao et al. 1997), and an area adjacent to the Red Sea Rift Zone (Wolfe et al. 1999; Hansen et al. 2006) have not found extension-parallel fast directions. This

suggests that flow in the asthenosphere is not completely driven by surface tectonics.

The anisotropic signature beneath continental rift zones can provide important constraints on the mechanism of extension. For example, a passive model of continental rifting, where the entire lithosphere is extended below the rift, would be expected to produce a lattice preferred orientation (LPO) of olivine aligned parallel to the direction of extension. Active rifting involving thinning of the lithosphere through small-scale convection might result in more complex flow and therefore more complicated LPO alignments, depending on the details of the small scale convection. In addition to LPO developed during mantle flow, alternative models for seismic anisotropy beneath rift zones include fossil LPO frozen into the lithosphere during a previous tectonic event and the alignment of magmatic cracks. These magma-filled cracks are expected to align themselves perpendicular to the east compressive stress direction, resulting in rift-parallel fast polarization directions. This mechanism is analogous to extensive dilatancy anisotropy, where parallel alignment of vertical, fluid-filled microcracks in the crust produces anisotropy. It has been suggested as the dominant cause of anisotropy beneath the Rio Grande and East African Rifts (Gao et al. 1997).

Results of previous research found a fast polarization direction parallel to the Red Sea Rift's spreading, by modeling far-regional surface waves (Schwartz et al. 2000). That study estimated crustal and upper mantle velocity structures for the Red Sea Rift Zone that were derived by modeling regional and far-regional body and surface waveforms. The best-fit model had a 17 km thick crust with anomalously low upper mantle velocities ($V_p = 7.7$ km/s) underlain by a significant low velocity zone. Velocity models that fit the radial and vertical waveforms are unable to accurately predict the Love wave on the transverse component. Including 3–4 % faster SH than SV velocities in the upper mantle replicates the Love wave and points to a fast anisotropic polarization axis parallel to the rift's spreading direction. These results are in direct contradiction to the SKS splitting results of Wolfe et al. (1999) and require further investigation of the anisotropic structure beneath the Red Sea Rift zone to understand its origin and relationship to the geodynamic processes involved in continental rifting.

Here we used the KACST data set to address this very important problem. Specifically, we measured teleseismic shear wave splitting in S and SKS phases recorded by 26 broadband stations of the KACST network that border the Red Sea in Saudi Arabia. The S and SKS splitting parameters were analyzed for the possibility of lateral variations in anisotropic structure and dipping symmetry axes. Dipping

symmetry axes were not considered in any of the previous studies of rift zone anisotropy, but may be able to reconcile the apparent difference in fast polarization directions obtained from body and surface waves for the Red Sea Rift Zone. Regional and far-regional surface waves from moderate sized events in the Red Sea region recorded by all available stations in the area were modeled to increase the surface wave observations and confirm or refute our previously obtained extension-parallel fast propagation direction. The S, SKS, and surface wave anisotropy results were combined in an attempt to construct a consistent model for mantle flow beneath this rift zone.

The study of Wolfe et al. (1999) as well as most shear-wave splitting studies concentrate on the SKS phase and average individual splitting measurements (fast polarization directions and delay times) made from events at various back-azimuths to obtain station averages. SKS is the favored phase because it passes through the liquid outer core and any effects of source-side splitting are obliterated due to its complete conversion to compressional motion in the outer core. This property of outer-core-traversing waves renders them very powerful to study receiver side anisotropy. The tendency to average individual splitting parameters is primarily due to the relatively small number of observations at each station (since SKS phases alone are favored) and large measurement errors. Averaging splitting parameters implicitly assumes that the anisotropy is adequately described by a single anisotropic region of hexagonal symmetry with the olivine axes oriented horizontally, thus implying horizontal flow. This may not always be a valid assumption, so rather than averaging individual splitting parameters obtained from different events to produce station averages, we analyzed the dependence of splitting parameters on arrival directions. This allowed us to determine: 1) if waves from different directions sample different anisotropic regions; and 2) if the anisotropic medium has a symmetry that is more general than hexagonal with a horizontal symmetry axis.

Although S phase splitting is more difficult to interpret than SKS, since its splitting could have occurred anywhere along its propagation path, the inclusion of S phases greatly increases the range of available incidence angles and back azimuths and allows interpretation of individual splitting measurements. We incorporate S-wave splitting in this study and remain aware of the possibility of source-side anisotropy for the S phases. We however, preferably analyzed S phases from deep focus events to minimize this effect. We used the horizontal velocity traces to obtain the splitting parameters. For SKS phases we rotated and shifted the two components to find those parameters (polarization direction, phi and delay time) that minimize the energy on the transverse component and render the particle motion most linear, that

is, we minimized the smallest eigenvalue of the covariance matrix. For S we used this covariance method. Measurement errors were estimated by the commonly used F test method.

Regional and Far-Regional Surface Wave Modeling

While knowledge of the velocity structure of northeastern Africa is important for understanding its tectonic development, progress has historically been hindered by both a lack of large African earthquakes and the sparseness of seismic stations at regional distance from seismic sources. Although large African earthquakes are still quite rare, station coverage in the area of the Red Sea Rift is now sufficient for regional waveform modeling of relatively pure paths traversing the Red Sea. We tested and refined our previously derived model of the crust and upper mantle structure beneath the Red Sea Rift zone through waveform modeling at regional and far-regional distances. Events with high signal to noise with known focal mechanisms were culled to insure that the data possess distinct compressional, shear, and surface wave arrivals. Processing and modeling of the data were done following procedures used by Rodgers and Schwartz (1998) and Rodgers et al. (1999) and include: (1) deconvolution of the station response to ground displacement; (2) initial band-pass filtering between 5 and 100 s; (3) rotation of horizontal components to the great-circle coordinates; and (4) application of a grid-search algorithm to determine crustal and mantle parameters that best-fit both the surface and body waves in the period ranges between 20 and 100 s.

Modeling surface and body waves together provides better constraints upon the crustal and upper mantle structure than modeling selected portions of the seismograms because it includes information about the surface wave group and phase velocities plus the body wave arrival times and their relative amplitude to the surface waves. Using a range of velocity and layer thickness parameters, a suite of models is created and synthetic reflectivity seismograms (Randall 1994) generated for each. The best parameters are chosen by calculating a normalized least-squares misfit between the data and synthetic components. Initial iterations focus on constraining the crustal velocities and thickness through fitting the absolute timing, amplitude, and dispersion of the Love and Rayleigh surface wave packets. Later iterations involve varying lid and upper mantle thickness and gradients, allowing shear velocity to increase independently of the P/SV velocity structure if necessary to fit the transverse and radial component surface waves and the P and S body wave arrivals and amplitudes.

Data Analysis and Results

Teleseismic Travel Time Tomography

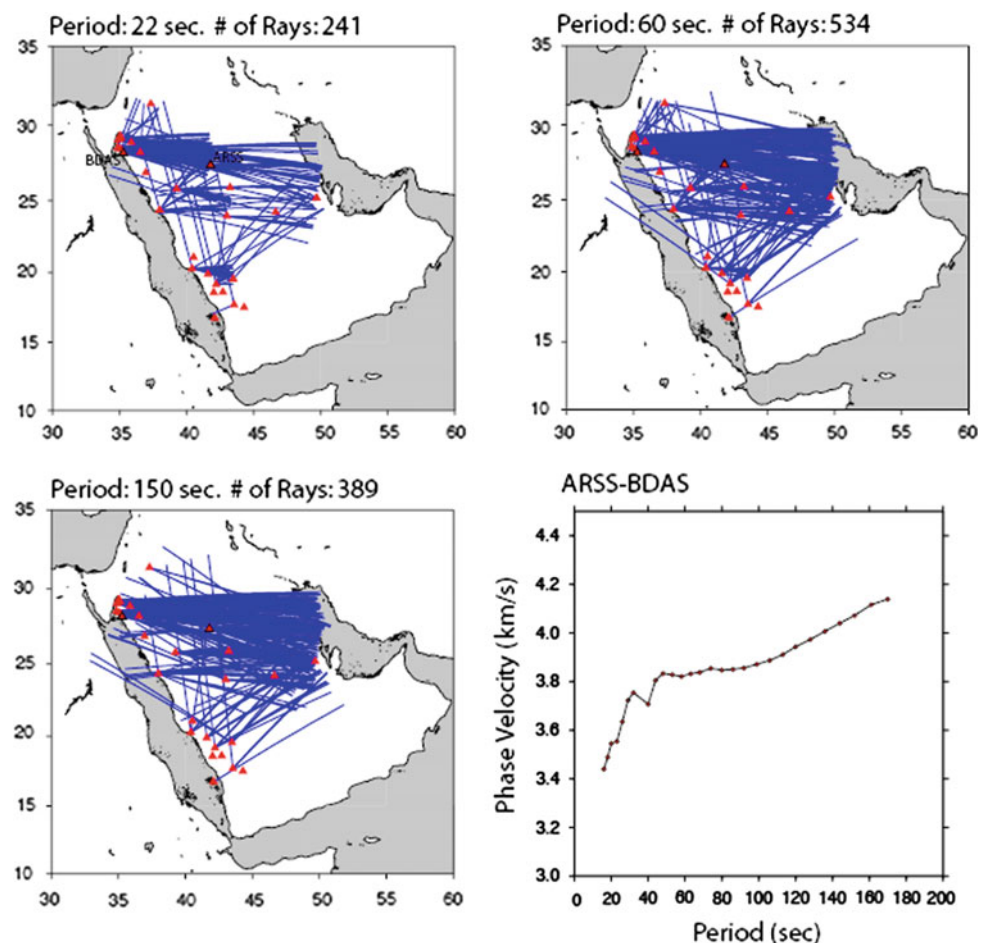
We determined detailed models of compressional and shear velocities of the crust and upper mantle down to about 400 km using teleseismic receiver functions and P- and S-wave travel time tomography. The state of strain in the upper mantle was determined from teleseismic shear wave splitting. Deep receiver functions were sampled for the upper mantle transition zone discontinuities at 410 and 660 km. The resulting models provided new constraints on tectonic models of the rupturing of continental lithosphere and the source of volcanism in the Arabian Shield.

Rayleigh wave dispersion curves were measured using the array methods of Menke and Levin (2002) as shown in Fig. 5. The figure shows path coverage for three period bands centered at 22, 60 and 150 s. The fourth panel shows the Rayleigh wave dispersion curve for the inter-station path between KACST station (ARSS) and BDAS in Ethiopia. The coverage is quite good for this data set (Park et al. 2005).

In this study, the tomographic inversion method uses a multi-channel cross-correlation (VanDecar and Crossen 1990) to find the optimal set of relative delays between teleseismic P-wave arrivals at the entire KACST network. Tomography requires many crossing ray paths in order to isolate the locations of velocity anomalies below the network. The method uses an iterative non-linear ray-tracing algorithm to allow for ray-bending 3-D structure. For the P-wave model, we used 401 earthquakes resulting in 3416 ray paths with P- and PKP-wave arrivals. The majority of the events are located in the western Pacific Rim between back azimuths of 15 and 150 degrees, but the events are distributed over a wide range of back azimuths (Fig. 6a). The waveforms were filtered with a zero-phase two-pole Butterworth filter between 0.5 to 2 Hz, and relative P-wave travel time residuals were computed (Park et al. 2005).

For the S-wave model, we used 201 earthquakes resulting in 1602 ray paths with S- and SKS-wave arrivals. Although the total number of rays for the S-wave model is half of the rays for the P-wave model, the event distribution shows better coverage of back azimuths (Fig. 6b). The signal processing procedures for S-wave are exactly same as for

Fig. 5 Rayleigh wave dispersion curves for three period bands centered at 22, 60, and 150 s. The fourth panel shows the Rayleigh wave dispersion curve for the inter-station path between KACST station ARSS and BDAS in Ethiopia



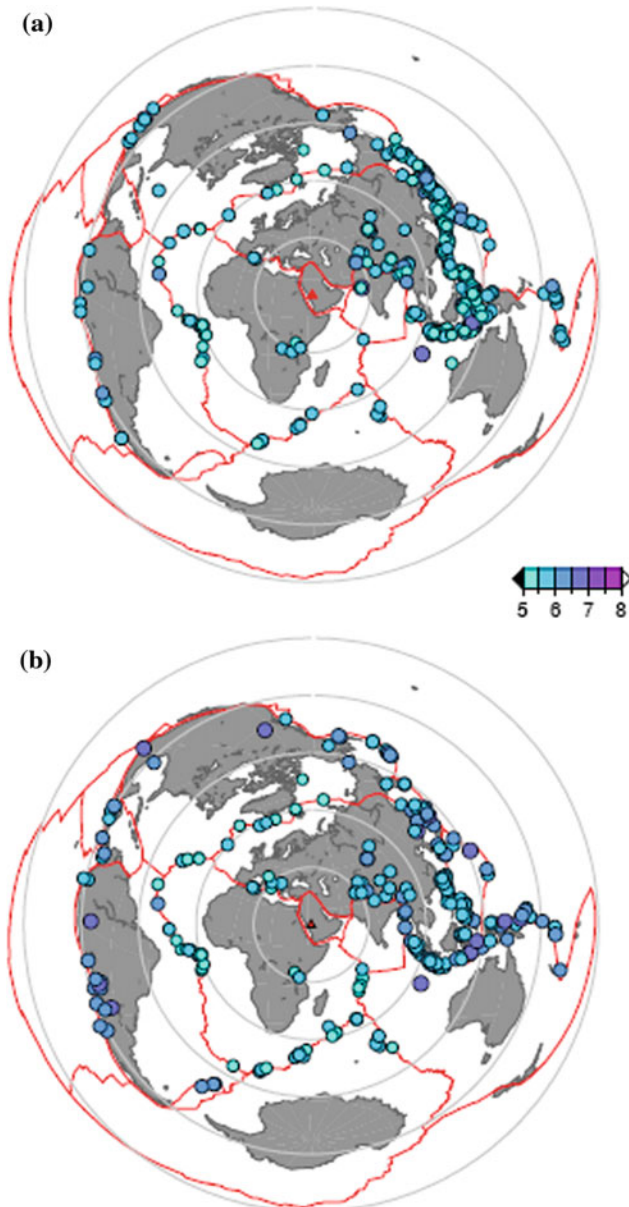


Fig. 6 The distribution of earthquakes for **a** P-wave (3416 rays from 401 events) and **b** S-wave (1602 rays from 201 events) events plotted by the equal distance projection. The color scale indicates the magnitude of each event, the *red solid lines* show plate boundaries, and each circle represents a 30° distance interval from the center of KACST seismic array

P-wave data, but traces are filtered with a lower frequency band (0.04 to 0.1 Hz) and relative arrival time residuals are computed by the multi-channel cross-correlation (MCCC) method with a fifteen-second time window (Park et al. 2005).

The resulting tomographic images of upper mantle structure at depths of 100–400 km are shown in Fig. 7. P-wave velocities vary by $\pm 2\%$ beneath Arabia where

slower velocities than average are generally beneath the Arabian Shield and faster than average velocities beneath the Arabian Platform. However, a striking feature is the low velocities extending through the upper mantle beneath the eastern edge of the Arabian Shield (beneath Riyadh). This feature can be seen in the cross-sections shown in Fig. 8.

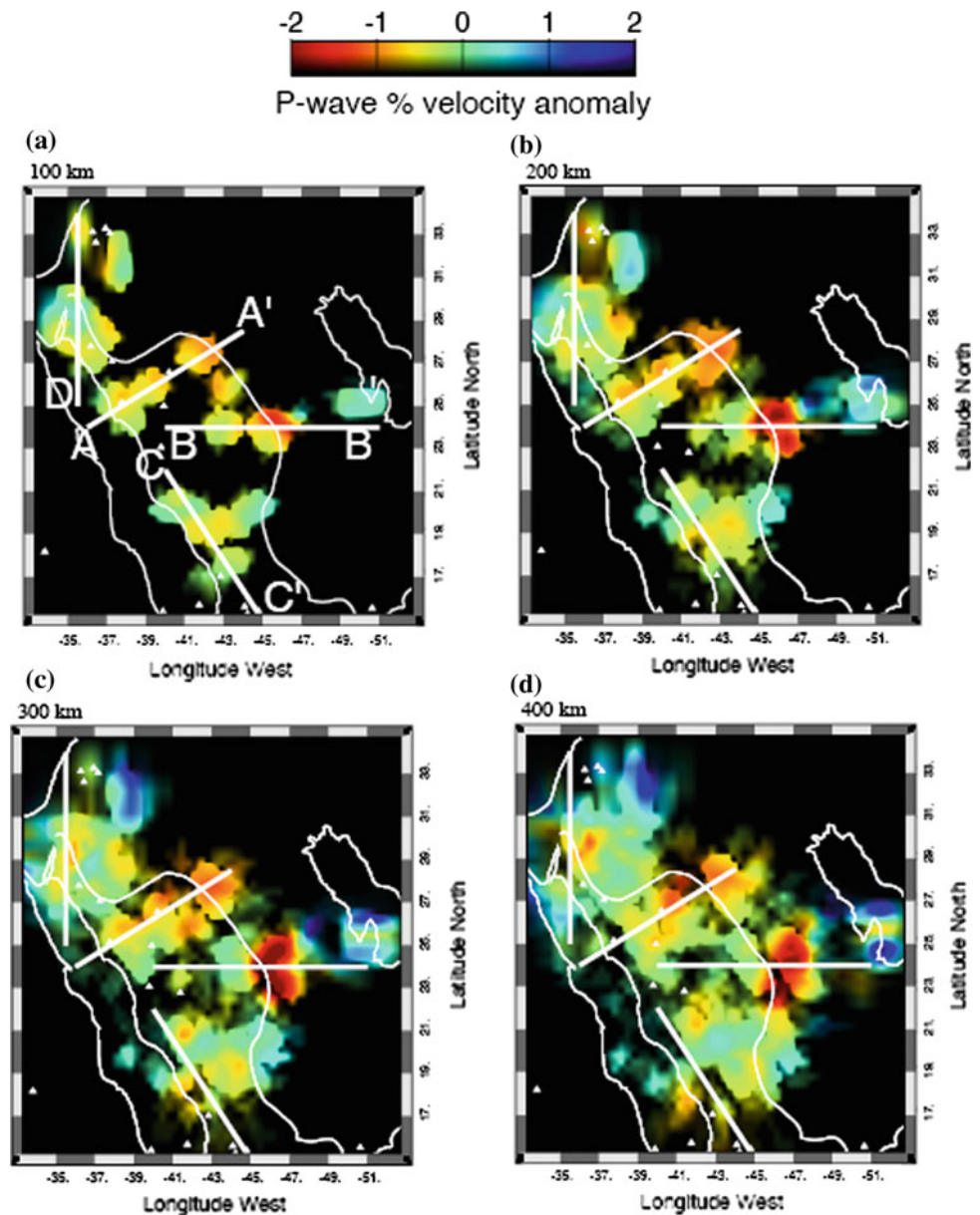
For comparison, we show the upper mantle P-wave velocity model of Benoit et al. (2003) in depth slice and cross-section view in Figs. 9 and 10, respectively. That study used data from the 9 station IRIS-PASSCAL Saudi Broadband Deployment (Vernon et al. 1996). In fact, the sampling is complementary, with the PASSCAL data covering north-south and northeast-southwest trending zones across the Arabian Shield beneath the stations. As can be seen in Figs. 9 and 10, the resolution and lateral extent of the area imaged using the Saudi Arabian Broadband Deployment (SABD) data sets are quite limited.

Resolution Tests

To test the resolution of our P- and S-wave model, we produced a synthetic checkerboard model consisting of 100 km diameter spheres with $\pm 5\%$ slowness anomalies placed at 100, 400, and 700 km depths (Figs. 11 and 12). Ray paths through a 1-D reference mode as defined by the IASP91 (Kennett and Engdahl 1991) are used, and noise is added to the synthetic travel-times as a Gaussian residual time error with a standard deviation of 0.02 and 0.04 s for the P- and S-wave data, respectively. Figures 11 and 12 show the recovered structure from the checkerboard test for P- and S-wave velocity perturbations, respectively. The input spheres are retrieved below 200 km depth (Fig. 11 e–h for P-wave tomography and Fig. 12 e–h for S-wave tomography), and the amplitudes of the slowness anomalies are recovered at $\sim 20\%$ of the input anomaly. Since the spacing of seismic stations is sparse, and the ray paths of teleseismic body-waves are incident vertically near the surface, the velocity perturbations set at 100 km depth were recovered with very small anomaly values in our model. However, the cross-section images of P- and S-wave models show that the patterns of the retrieved models are reliable between 200 km and 400 km depth (Figs. 11g, h and 12g, h).

Generally speaking, we would suggest that low velocities beneath the Gulf of Aqabah and southern Arabian Shield and Red Sea at depths below 200 km are related to mantle upwelling and seafloor spreading. Low velocities beneath the northern Arabian Shield below 200 km may be related to volcanism. The low-velocity feature near the eastern edge of the Arabian Shield and western edge of the Arabian Platform could be related to mantle flow effects near the interface of lithosphere of different thickness.

Fig. 7 P-wave velocities in the upper mantle at depths of **a** 100, **b** 200, **c** 300 and **d** 400 km depths. Velocities are plotted with the color scale as the relative perturbation to the average one-dimensional background model. The locations of cross-sections through the model are indicated by the white lines



Modeling of Surface Wave Dispersion

In this study we applied a new method to simultaneously fit receiver function and surface wave group velocity data (Tkalcic et al. et al. 2005). The method involves a combination of grid search, iterative inversions, and forward modeling to simultaneously explain the surface wave dispersion (from 7 to 100 s for Rayleigh and 20 to 70 s for Love waves) and teleseismic RF observations at the broadband stations in the Arabian Peninsula. For the grid search, we used a database of pre-calculated theoretical receiver functions and dispersion curves, which allowed us to significantly reduce the computing time and investigate a wide range of structural models. We initially fit receiver functions and shorter periods of the

observed dispersion curves with the structure within the crust and immediately beneath the crust. We then used an additional grid search to characterize the lithospheric lid and low velocity zone in the upper mantle, fixing the crustal structure and fitting longer period dispersion curves. The method proved to be robust and could be applied in the cases where little a priori knowledge exists about the crustal structure. Additionally, as a result of the “step by step” approach to recover the structure starting from the “top” and ending with the “bottom” of the model, the multi-step method revealed how mantle velocity variations and transverse isotropy is needed to simultaneously fit all available data.

We apply this technique to a number of stations that sample the complexity of tectonic environments and provide

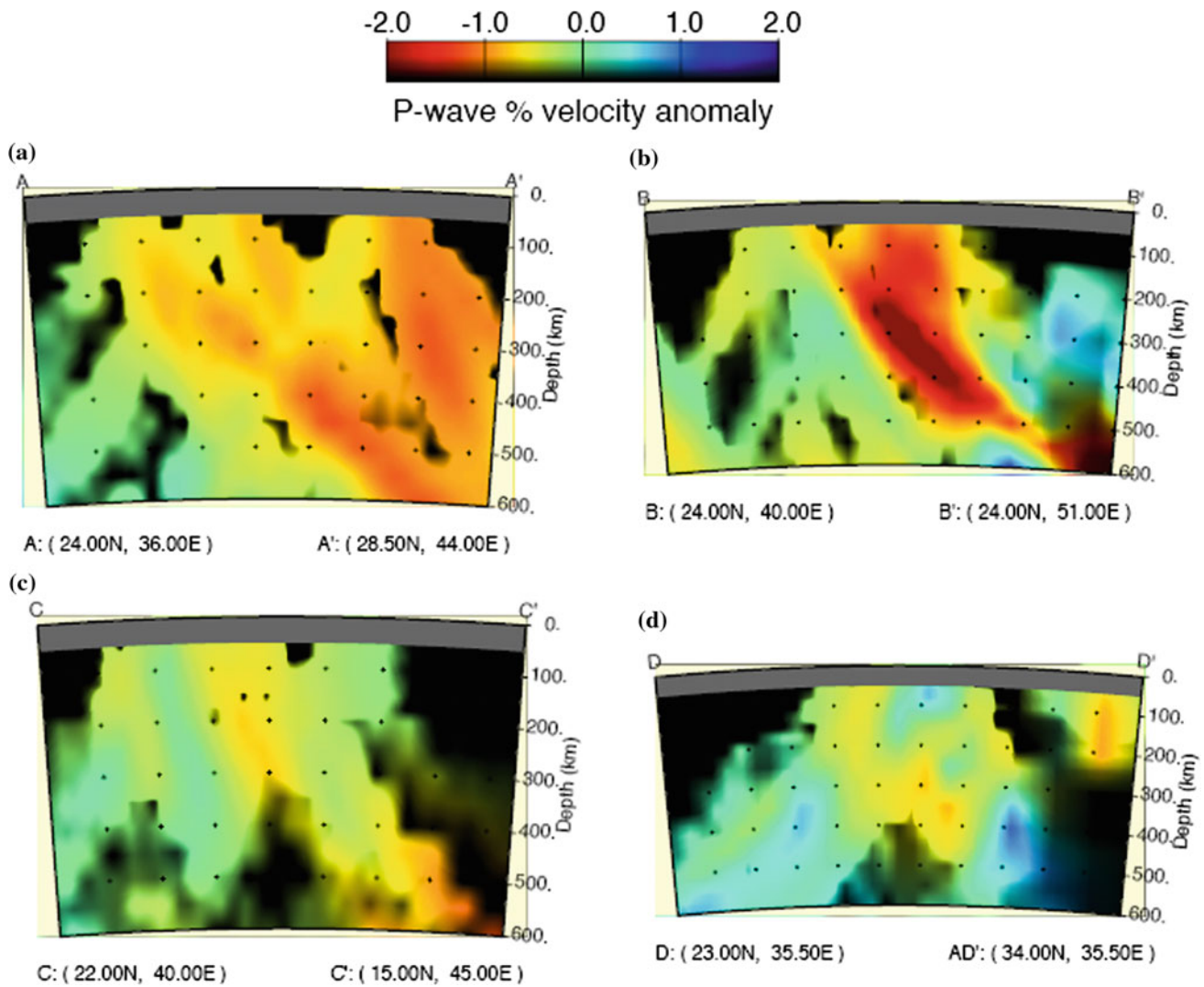


Fig. 8 Cross-sections through the upper mantle tomography model: **a** A-A' across the northern Arabian Shield; **b** B-B' across the shield-platform boundary; **c** C-C' along the southern Red Sea coast (Asir Province); and **d** D-D' along the Gulf of Aqabah and the Dead Sea Rift

new constraints on structure. Figures 13, 14, 15, and 16 illustrate the final fit to the data and our best models for stations ARSS, BLJS, NAMS, and YNBS, respectively. In the following, we discuss the features of these models.

Station ARSS (Fig. 13) is located on the eastern edge of the Arabian shield. Our final model has a 40 km thick crust and a relatively pronounced Moho, with a thin lithospheric lid extending 10 km below the Moho. No transverse isotropy is needed to explain simultaneously the RFs and surface-wave dispersion data. It appears that the lithospheric lid thickens significantly and that the slight transverse isotropy does not exist at ARSS.

The velocity structure for station BLJS (Fig. 14) is characterized by shallow low velocities, normal crustal velocities, and a Moho depth of 38 km. The mantle is characterized by a thin lid and decreasing velocities, and up

to 5 % anisotropy ($v_{SV} > v_{SH}$). These results are consistent with the nearby station, NAMS.

We observe a strong contrast in the velocity at the Moho for station NAMS (Fig. 15). The crustal thickness of 41 km is in agreement with the estimate of Al-Damegh et al. (2005). The mid-crustal structure is characterized by a transition from slow to fast shear-wave speeds (exceeding 4 km/s) and a sudden drop of velocities at about 23 km depth by 0.6 km/s. The lithospheric lid of about 20 km thickness, overlaying a broad low-velocity zone that extends to about 140 km depth, is a well-pronounced feature in the upper mantle.

Station YBNS (Fig. 16) lies in the northern part of the Red Sea coast. YNBS is a station with considerably thinner crust (28 km) compared to other stations modeled in this report, but is consistent with the results of Al-Damegh et al.

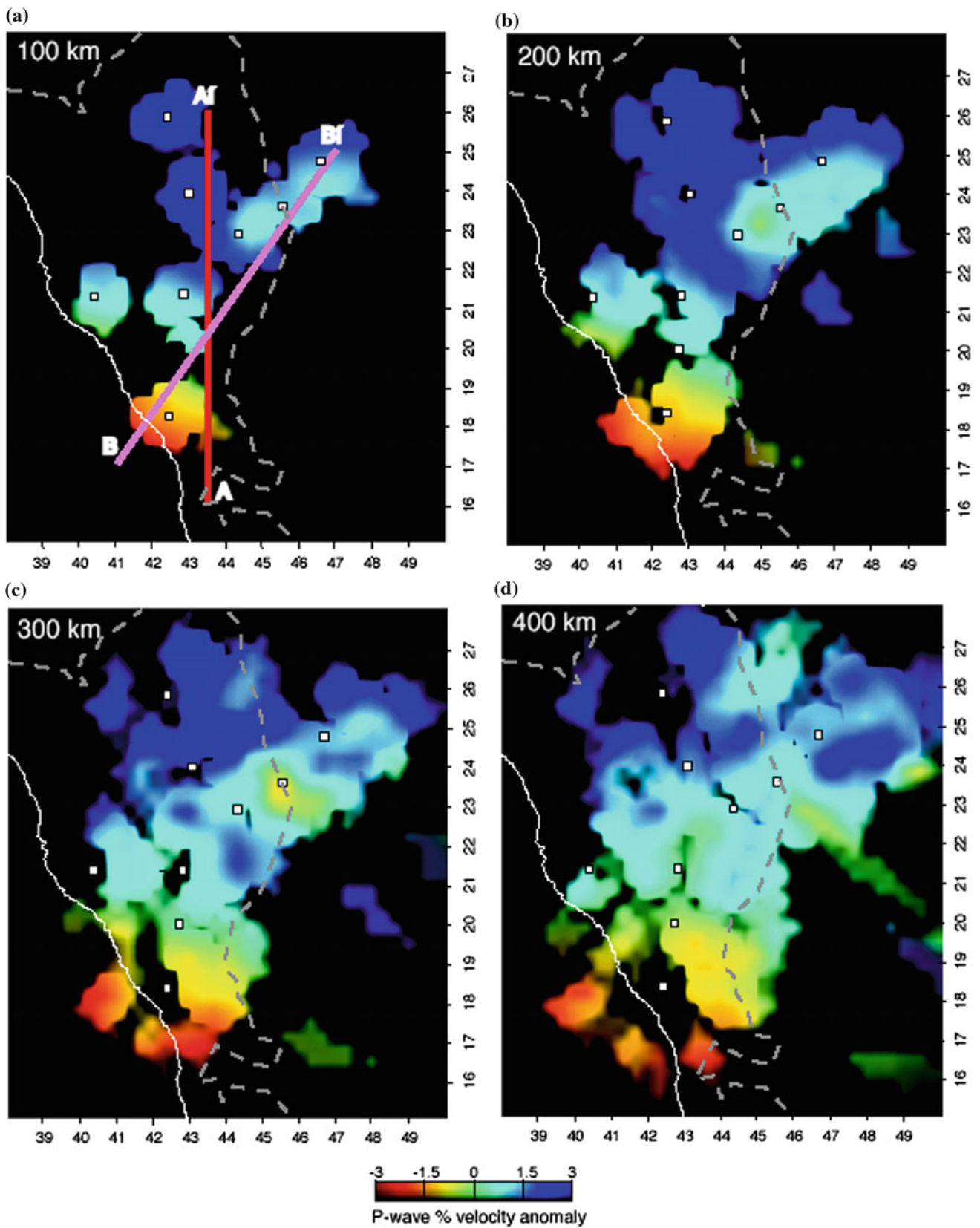
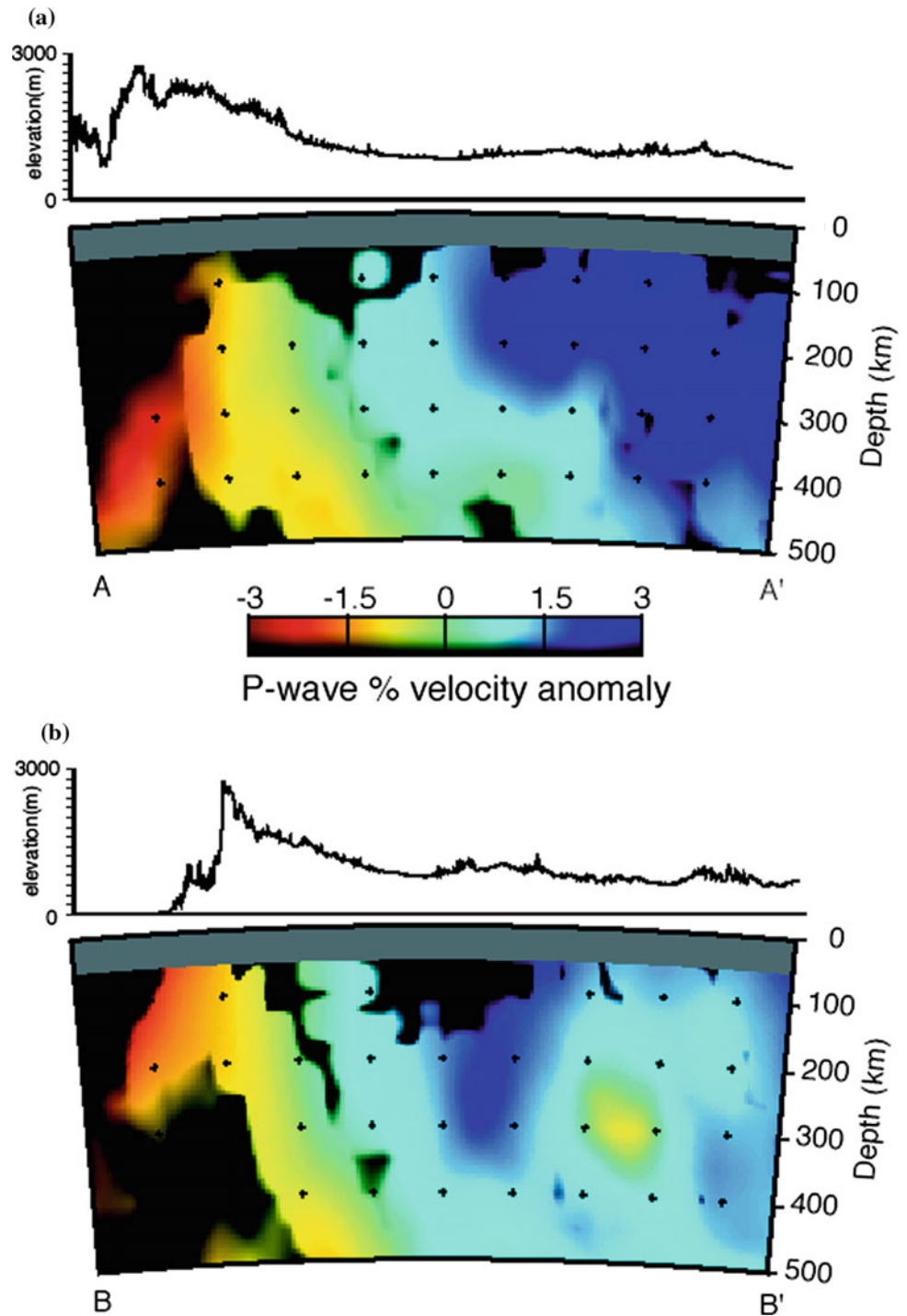


Fig. 9 Tomographic model of Benoit et al. (2003). P-wave velocities in the upper mantle at depths of **a** 100, **b** 200, **c** 300 and **d** 400 km depths. Velocities are plotted with the color scale as the relative

perturbation to the average one-dimensional background model. The locations of cross-sections through the model are indicated by the red lines

Fig. 10 Cross-sections through the upper mantle tomography model: **a** A-A' north-south section across the Arabian Shield and **b** B-B' southwest-northeast section from the Red Sea across the Arabian shield to the Arabian platform



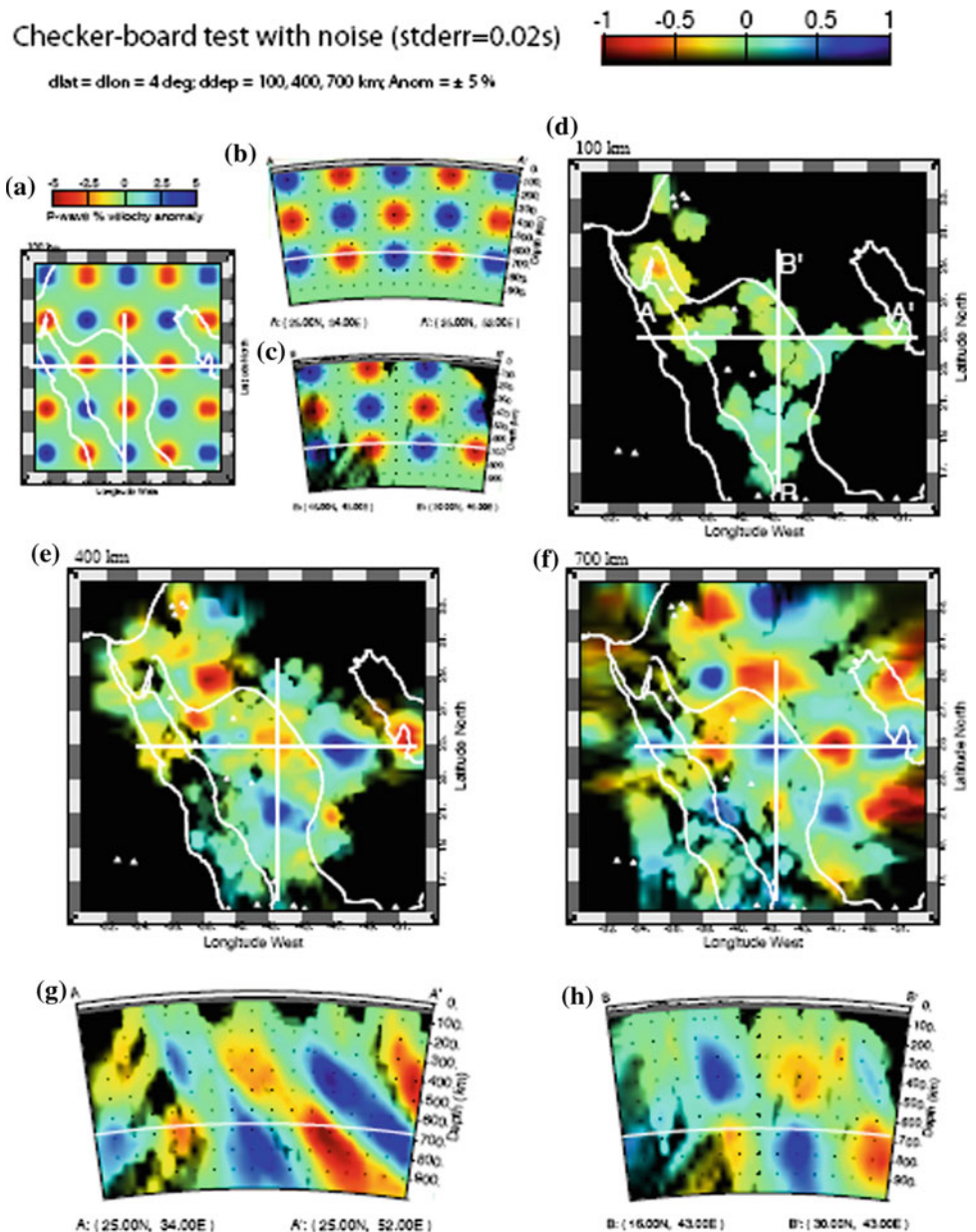
(2005). The mantle velocity is low (4.2 km/s on average), and no lithospheric lid could be observed in the final model (although a strong v_{SH} lid is required). The sign of anisotropy is thus opposite from the sign modeled for stations BLJS and NAMS in the southern part of the Red Sea.

We suggest that low velocities beneath the Gulf of Aqabah and southern Arabian Shield and Red Sea at depths below 200 km are related to mantle upwelling and seafloor

spreading. Low velocities beneath the northern Arabian Shield below 200 km may be related to volcanism. The low velocity feature near the eastern edge of the Arabian Shield and western edge of the Arabian Platform could be related to mantle flow effects near the interface of lithosphere of different thickness.

The resulting velocity models beneath the Arabian Peninsula provide new constraints on crustal and upper

Fig. 11 Synthetic checker-board resolution test for the inverted P-wave model. **a** shows the 100 km depth profile of the input model, and **b, c** show the cross sections located on **(a)**. 100 km diameter spheres defined by Gaussian functions across their diameter of $\pm 5\%$ peak velocity anomaly are distributed in layers of depth 100, 400 and 700 km. **d, e, f** are the 100, 400 and 700 km depth profiles inverted from the input model, and **g, h** are the cross-sections



mantle structure. This study shows an average crustal thickness of the Arabian shield of 36 km for the stations used in this study. Three layers can be deduced from the final velocity model, which is consistent with models reported by Al-Amri et al. (2004).

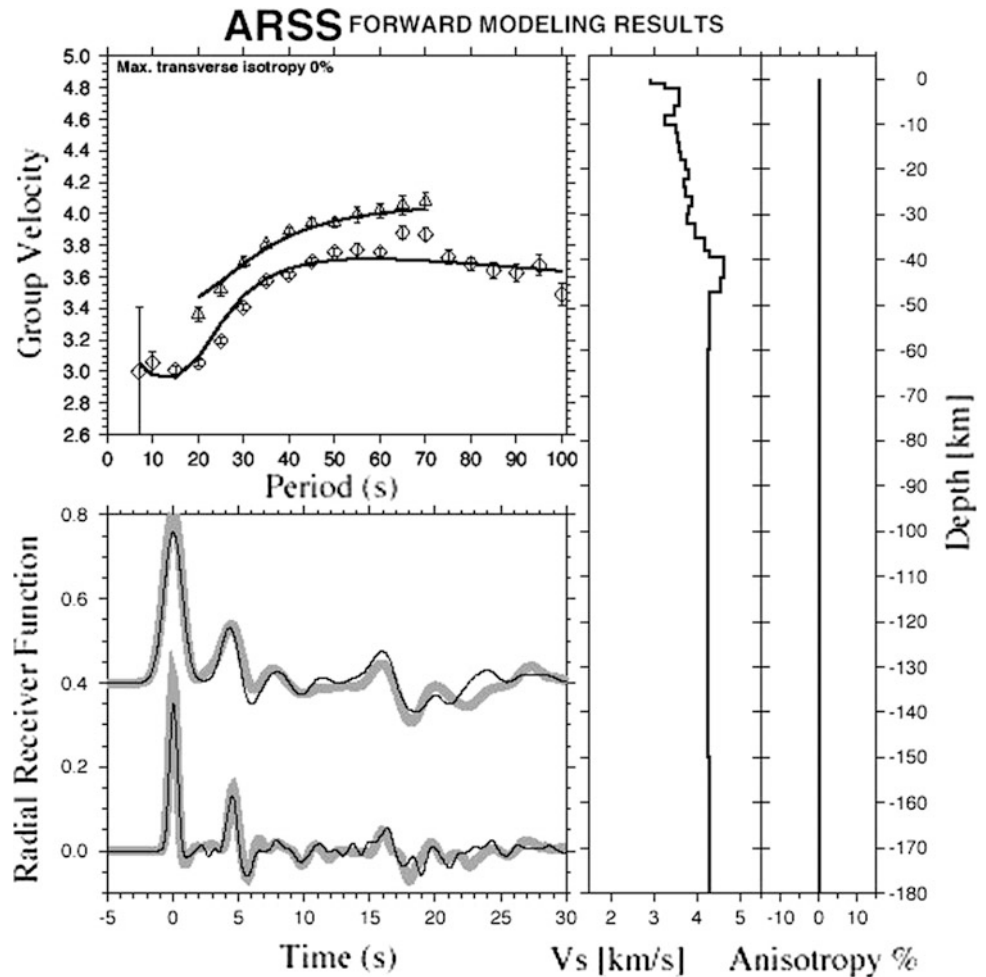
Generally speaking, the results for crustal structure are consistent with previous studies, where applicable. The new results for the lithosphere suggest that the mantle lithosphere is thin and the LVZ is significant near the Red Sea, where rifting is active. The mantle lid thickens away from the Red Sea in the Arabian interior. Furthermore, our results indicate the presence of polarization anisotropy in the lithospheric upper mantle, in the vicinity, as well as farther away from the Red Sea. Our modeling suggests $v_{SV} > v_{SH}$ in the

southern part of the Red Sea, consistent with vertical flow, and $v_{SH} > v_{SV}$ in the northern part of the Red Sea and the continental interior, as is commonly reported in the continents.

Mantle Anisotropy from Shear-Wave Splitting

Seismic anisotropy in the earth causes wave motions in different directions to travel at different speeds. For shear-waves, this can lead to bi-refringence, where different polarizations travel at different speeds. Furthermore, anisotropy can cause motions with one polarization to couple into other polarizations. The SKS phase is widely used to study

Fig. 13 Forward modeling of velocity and anisotropy structure in the upper mantle from Love and Rayleigh wave group dispersion for the ARSS station. The model shows the final fit to the data and no transverse isotropy is needed to simultaneously fit all available data



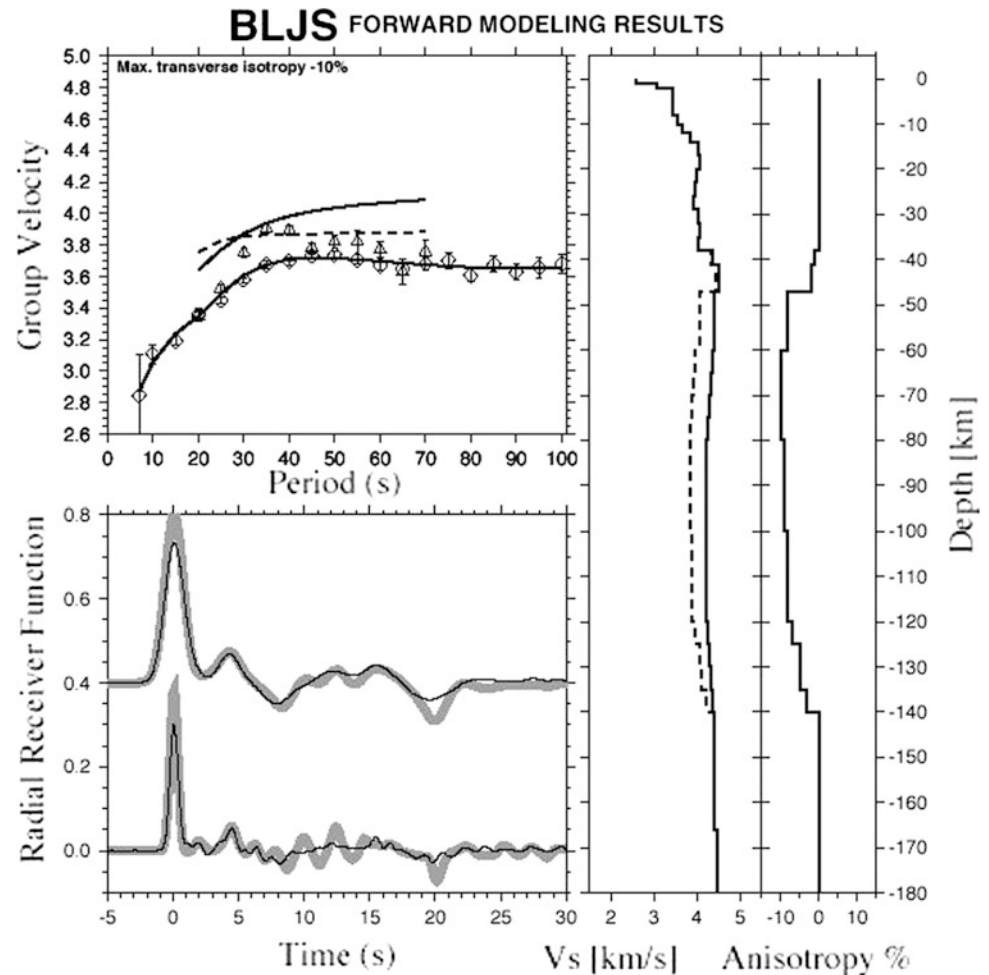
perpendicular to the Red Sea Rift and therefore does not support a passive rifting model. Also, the orientation of φ is at least 30° different from the reported absolute plate motion direction. It is possible that the anisotropic signature obtained could be the result of fossilized anisotropy in the lithosphere, where φ is aligned parallel to the northerly strike of accreted terranes and sutures dating back to the Proterozoic assembly of the Arabian platform (Stoeser and Camp 1985).

The results of Hansen et al. (2006) indicate a fairly consistent fast polarization direction of N20-25°W with delay times ranging between 0.75 and 1.2 s. This direction is similar but about 20° more westerly than the north-south fast polarization direction reported by Wolfe et al. (1999) from a temporary network of broadband sensors deployed over a much more spatially limited region of the Arabian Shield. The results of Hansen et al. (2006) extend and confirm their interpretation of a fairly homogeneous anisotropic fabric throughout the shield. However, Wolfe et al. (1999) could not discriminate between different interpretations of their dominantly north-south fast polarization directions. The

mechanisms that they considered included fossil anisotropy associated with formation of the Proterozoic Arabian lithosphere and modern mineral alignment caused by asthenospheric flow associated with the present northward motion of the Arabian Shield or with an Ethiopian mantle plume.

Generally, this study suggests that the observed splitting parameters are the result of a complex interaction of mantle flow in the asthenosphere. Shear caused by the absolute plate motion, which is directed approximately 40° east of north at about 22 mm/y (Fig. 18), may affect the alignment of mantle minerals. However, it has also been suggested that flow radiating from the mantle plume beneath Afar is channeled towards the Red Sea Rift (Ebinger and Sleep 1998), which is oriented approximately 30° west of north. Assuming that the strain caused by the plume flow is comparable to that of the plate motion, we can combine these two flow orientations, similar to the vector approach of Silver and Holt (2002). This gives an overall resultant that is oriented with a north-south alignment (Fig. 18). Our preferred interpretation of the slightly more westerly, and Red Sea Rift parallel, fast directions we obtained is the alignment of magma filled

Fig. 14 Forward modeling of velocity and anisotropy structure in the upper mantle from love and Rayleigh wave group dispersion for the BLJS station. The model shows the final fit to the data and up to 5 % anisotropy ($V_{sv} > V_{sh}$)



cracks that form perpendicular to the least compressive stress direction resulting in rift-parallel fast-polarization directions. This mechanism has been suggested as the dominant cause of anisotropy beneath other rift zones.

Seismic tomography models have shown that the upper mantle beneath the western portion of the Arabian Shield is anomalously slow, with velocities increasing towards the continental interior (Debayle et al. 2001; Benoit et al. 2003). These observations are attributed to thermal differences beneath Saudi Arabia and indicate a much hotter mantle beneath the Red Sea than beneath the interior of the shield, which is consistent with plume flow directed beneath the rift. Surface wave and receiver function analysis shows that there is a change from vertical flow in southwest Saudi Arabia to horizontal flow further north, also consistent with the presence of channelized flow from the mantle plume (Tkalcic et al. 2005). Daradich et al. (2003) demonstrated that the higher elevations along the Red Sea Rift and the overall tilt of the Arabian plate result from viscous stresses associated with large-scale mantle flow from the Afar plume. In addition, Schilling et al. (1992) found isotopic evidence for

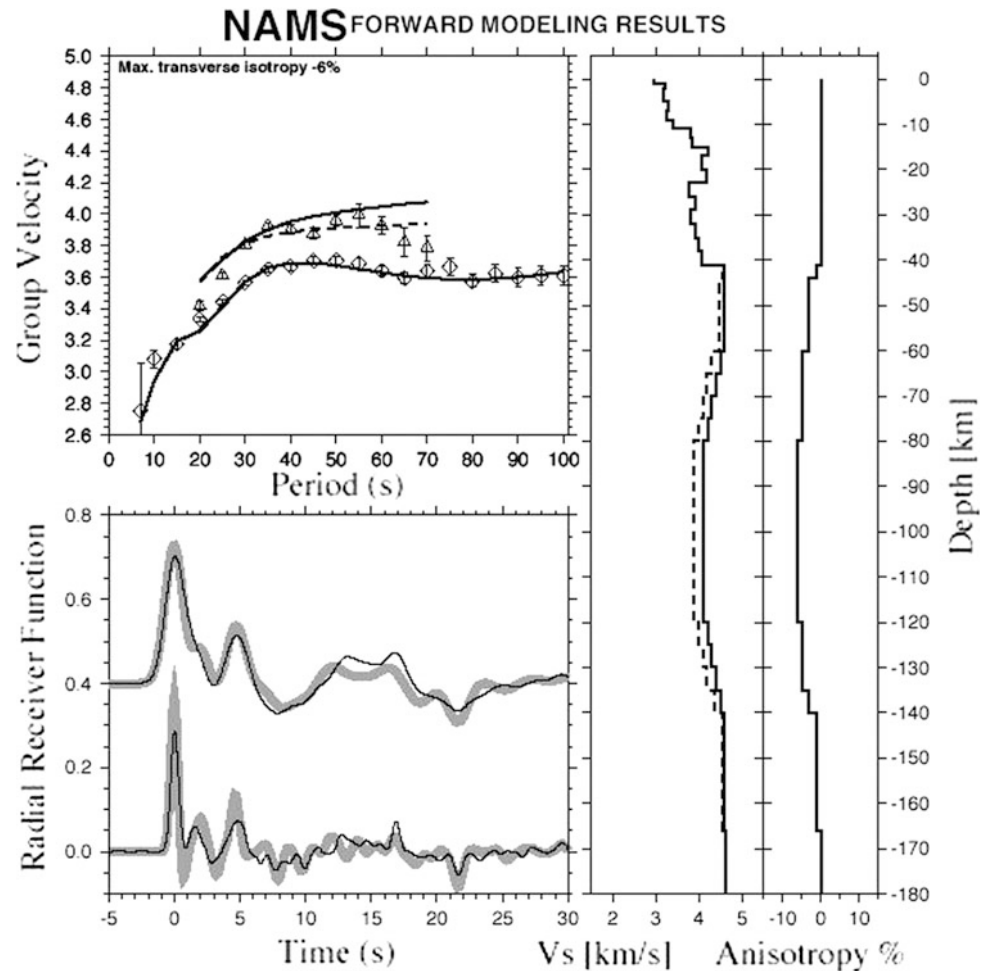
mantle mixing between a depleted asthenosphere and plume flow in Saudi Arabia, supporting the idea that an interaction of flows is occurring at depth. This combination of both plate and density driven flow can explain the observed anisotropic signature and is consistent with an active rifting model.

Discussion and Conclusions

Teleseismic data recorded on broadband instruments from four different seismic arrays were used in this study. The largest array of instruments used is the KACST and SGS seismic networks. To supplement the coverage, we also analyzed data recorded by the eight IRIS-PASSCAL Saudi Arabian Broadband Array stations, which operated from November 1995 to March 1997, RAYN/GSN data, data from two stations deployed in Jordan, and data recorded by two stations in the UAE.

S-waves with high signal-to-noise ratios were selected from earthquakes with magnitudes larger than 5.7 in a distance range of 60° to 85° . Waveforms were first rotated from

Fig. 15 Forward modeling of velocity and anisotropy structure in the upper mantle from love and Rayleigh wave group dispersion for the NAMS station. The model shows the final fit to the data. A broad transverse isotropy coinciding with the low velocity zone in the mantle is required with V_{sv} exceeding V_{sh} by 6 %

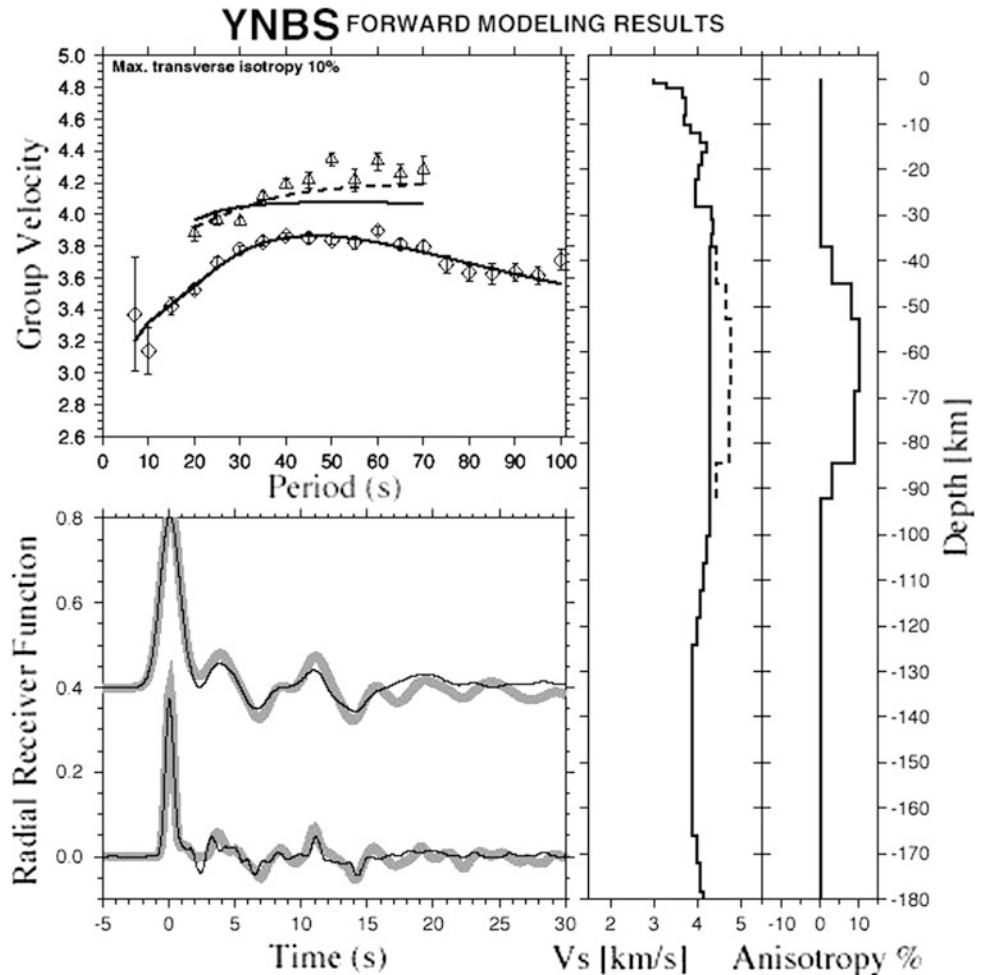


the N-E-Z to the R-T-Z coordinate system using the event's back-azimuth and were visually inspected to pick the S-wave onset. The three-component records were then cut to focus on the section of the waveform that is 100 s prior to the S-wave onset and 20 s after. To more clearly detect Sp conversions, the cut R-T-Z data must be further rotated around the incidence angle into the SH-SV-P coordinate system and deconvolved. This second rotation is critical because if an incorrect incidence angle is used, noise can be significantly enhanced and major converted phases may become undetectable. A subroutine was developed, based on the approach of Sodoudi (2005), which rotates the cut R-T-Z seismograms through a series of incidence angles, from 0° to 90° in 3° increments, to create a set of quasi-SV and quasi-P data. Each quasi-SV component is then deconvolved from the corresponding quasi-P component using *Ligorria and Ammon's* iterative time domain method, which creates an SRF. To make the SRFs directly comparable to PRFs, both the time axes and the amplitudes of the SRFs must be reversed. Using this approach, 31 different SRFs, corresponding to the 31 different incidence angles examined, are created for each event at a given station.

To limit our examination to the true P-SV components and their corresponding receiver function, we found the incidence angle that minimizes the direct S-wave energy on the P-component. On the time-reversed receiver functions, the direct S arrival is at 0 s. Therefore, we are only interested in the receiver function whose mean amplitude is closest to zero at zero time. A second subroutine was developed to examine all the generated receiver functions for a given event and determine which record best meets this criterion. The P-SV components and the corresponding receiver function with the appropriate incidence angle are retained, and the remaining records are discarded.

Once receiver functions were generated for all events at an examined station, a move-out correction was applied to the receiver functions to correct for variations in distance between events. Again, to make the SRFs directly comparable to PRFs, we used a reference slowness of 6.4 s/deg. Each individual receiver function is then visually inspected and compared to previously determined PRFs at the same station to identify the Moho phase. Only SRFs that display a clear Moho conversion at the appropriate time are used for further analysis. These records were then stacked to obtain a

Fig. 16 Forward modeling of velocity and anisotropy structure in the upper mantle from love and Rayleigh wave group dispersion for the YNBS station. The model shows the final fit to the data. A strong transverse isotropy is found (8 % of $V_{sh} > V_{sv}$)



better signal-to-noise ratio for the weaker LAB phase (Lithosphere/Asthenosphere Boundary).

It should be noted that a similar approach to that outlined above was also used to examine SKS arrivals. In this case, we examined earthquakes with magnitudes larger than 5.6 in a distance range from 85° to 120° . However, it was discovered that the SKS arrivals do not generate clear Sp conversions given their steeper angles of incidence. Therefore, further examination of SKS receiver functions was not pursued.

Synthetic receiver functions were generated using the reflectivity method to match the amplitude and timing of both the Moho and LAB conversions on the stacked SRFs. Using the programs "icmod" and "respknt", the responses of an incoming S-wave to different three-layer velocity models were generated. These synthetic responses were then processed using the same approach outlined previously to obtain the synthetic SRFs. The amplitude and timing of the phases on the real and synthetic receiver functions were matched by adjusting the crustal, upper mantle, and lower mantle velocities as well as the depth of the Moho and the

LAB. While these values varied from station to station, the average crustal and upper mantle S-wave velocities needed to fit the Moho amplitude were about 3.6 and 4.5 km/s, respectively. These are similar to the S-wave velocities used to fit the Moho amplitude on the SANDSN PRFs. To fit the LAB amplitude, an average lower mantle velocity of about 4.2 km/s is required. In all cases, a default Poisson's ratio of 0.25 was used.

It should be noted that the average shear velocities and default Poisson's ratio used to generate the synthetics differ from those found by waveform modeling. Rodgers et al. (1999) reported average crustal S-wave velocities of 3.7 and 3.5 km/s and average upper mantle S velocities of 4.3 and 4.55 km/s for the Arabian Shield and Platform, respectively. In addition, the reported Poisson's ratio in the Arabian Shield mantle was 0.29, while in the Platform it was 0.27. Testing revealed that the waveform modeling velocities did not fit the SRF phase amplitudes as well, but the timing of the phases only changed by a few tenths of a second. Therefore, the difference in shear velocities only leads to a few kilometers difference in depth. However, the timing of

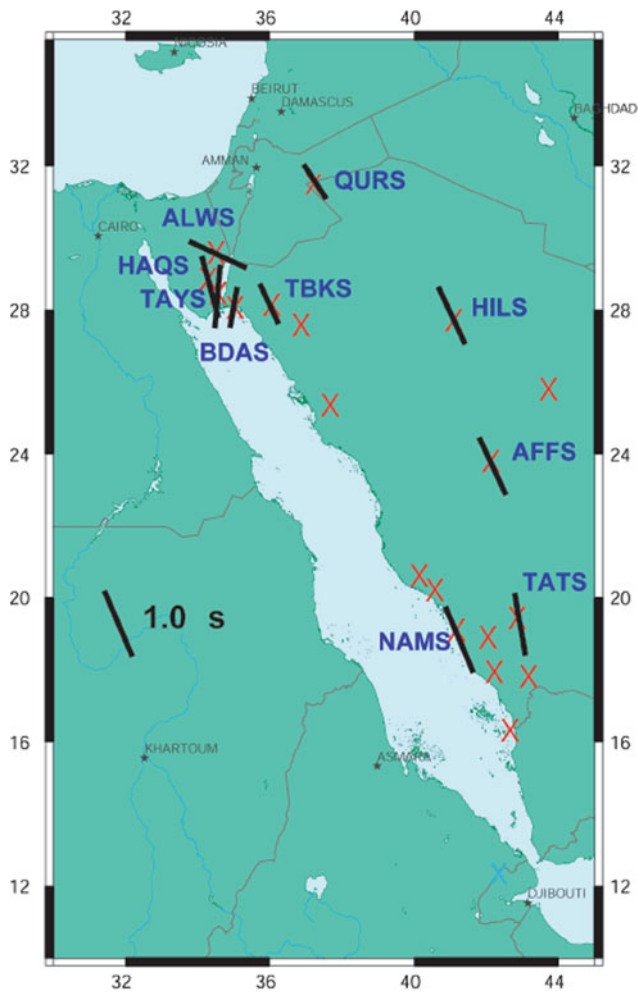


Fig. 17 SKS splitting parameters for several KACST stations. *Red crosses* indicate station locations with too few SKS splitting parameters to determine a meaningful average. The direction of the *black bar* indicates the average direction of fast polarization and its length is scaled by the delay time between the fast and slow waves. Most stations east of the Red Sea Rift show consistent northwesterly fast directions with some complications arising in the vicinity of the Dead Sea

the phase conversions is more dependent on the Poisson's ratio. Larger Poisson's ratios, such as those suggested by the waveform modeling, results in earlier arrivals and hence shallower depths. Several tests were performed to examine how much the Moho and LAB depths changed when using the Shield and Platform Poisson's ratio values. Based on the amount of variation observed, the reported Moho and LAB depths are accurate to within 5 and 10 km, respectively.

Seafloor spreading in the Red Sea is non-uniform, ranging from nearly 0 cm/year in the north to about 2 cm/year in the south. Given the configuration of stations, we focused our examination along profile AA', which extends from the southern Red Sea Rift axis inland to station HASS (Fig. 19). This allowed us to examine the most extensively rifted portion of the lithosphere as well as the structure beneath

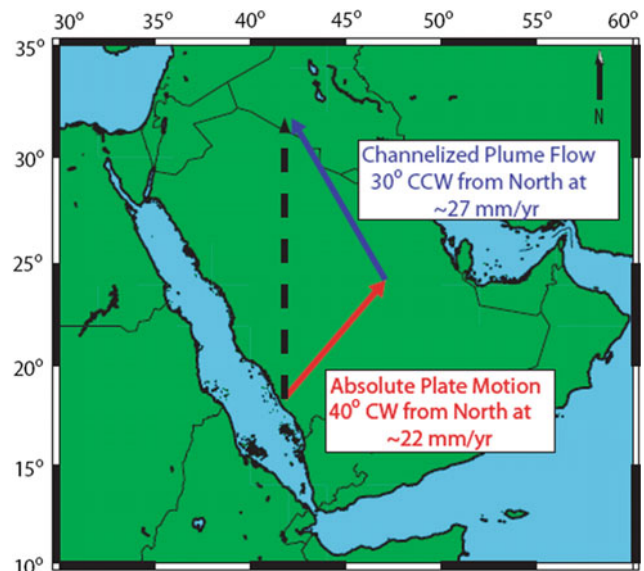


Fig. 18 Vector analysis of plate motion (*red arrow*) coupled with channelized upwelling flow (*blue arrow*) beneath Saudi Arabia. If we estimate that absolute plate motion is oriented N40E at a rate of 22 mm/year and that channelized hotspot flow is oriented approximately N30W, then the rate of hotspot flow needed to obtain a north-south resultant (*black dashed arrow*) is ~ 27 mm/year

both the Arabian Shield and Platform. However, for comparison, we also examined the more northern profile BB', which extends from the northern rift axis across the Arabian Shield to station ARSS.

Similar to profile AA', the Moho and LAB along BB' are shallowest near the Red Sea and become deeper towards the Arabian interior. Near the coast, the Moho is at a depth of about 22–25 km. Crustal thickening continues until an average Moho depth of about 35–40 km is reached beneath the interior Arabian Shield. The LAB near the coast is at a depth of about 55 km; however, it also deepens beneath the Shield to attain a maximum depth of 100–110 km. These boundary depths are comparable to those at similar distances along profile AA' (Hansen et al. 2007).

The lithospheric structure along profile BB' was also tested by comparing its predicted gravity signature to data collected by the GRACE satellites (Fig. 20). The same density values for the Arabian Shield used in the examination of profile AA' were employed. In addition, since profile BB' has fewer stations and therefore fewer constraints, we set the lithospheric thickness beneath the rift axis to be similar to that on profile AA' and examined if the calculated gravity signature is consistent with the recorded data. Small-scale recorded gravity observations can be matched very well by slightly adjusting the Moho and LAB boundaries (within the estimated error). Broad-scale gravity observations are also fitted well by a shallow asthenosphere beneath the Red Sea. These results demonstrate that while

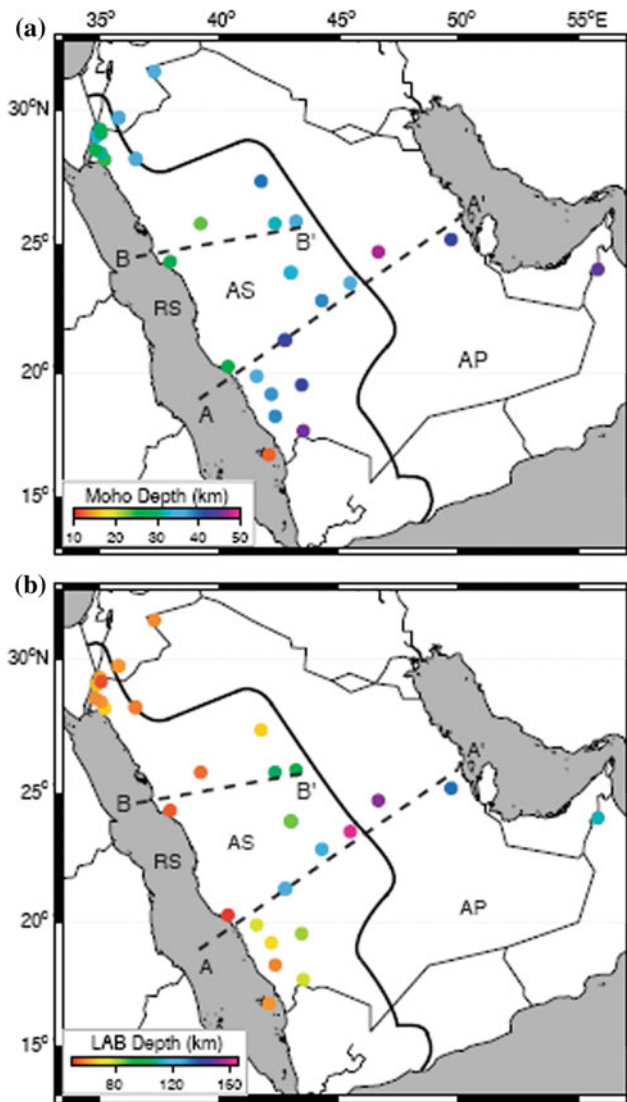


Fig. 19 Maps showing the boundary depths beneath Arabia. The colored circles show the **a** Moho and **b** LAB depths beneath individual stations, where warmer colors indicate shallower depths than cooler colors. The solid line marks the boundary between the Arabian shield (AS) and the Arabian Platform (AP) while the two dashed lines mark the locations of cross-sectional profiles AA' and BB'. The shallow (40–60 km) LAB along the Red Sea coast and Gulf of Aqabah thickens (80–120 km) toward the interior of shield with a step (20–40 km) across the Shield-Platform boundary (Hansen et al. 2007)

seafloor spreading is not as developed in the northern Red Sea, the lithosphere has still been thinned and eroded by rifting processes (Hansen et al. 2007).

Crustal Structures

Al-Amri et al. (2004) performed a grid search using travel time data sets: (a) Pn and Pg, and (b) Pn, Pg, and Sg. In order to select a single velocity model to be representative of the

paths sampled, they made use of the results of a seismic refraction study (El-Isa 1990; Seber et al. 1997). Their grid search results with the thicker crusts (28–30 km) are consistent with these earlier studies. The preferred model has a crustal thickness of 28 km for the Gulf of Aqabah (Table 1).

Earlier work with waveform data from the 1995–1997 Saudi Arabian Broadband Deployment by the University of California, San Diego (UCSD), and King Saud University resulted in models for the Arabian Platform and Arabian Shield (Rodgers et al. 1999). In that study, Love and Rayleigh wave group velocities were modeled to estimate average one-dimensional seismic velocity models of the two main geologic/tectonic provinces of Saudi Arabia. A grid search was used to quickly find a range of models that satisfactorily fit the dispersion data, then this range of models was explored to fit the three-component broadband (10–100 s) waveforms. The resulting models revealed significant differences between the lithospheric structures of the two regions (Tables 2 and 3).

To check the validity of the Arabian Platform model, we measured Rayleigh and Love wave group velocities for a number of regional events from the Zagros Mountains and Turkish-Iranian Plateau. Paths from these events to the SANDSN stations sample the Arabian Platform.

Generally, we would suggest that low velocities beneath the Gulf of Aqabah and southern Arabian Shield and Red Sea at depths below 200 km are related to mantle upwelling and seafloor spreading. Low velocities beneath the northern Arabian Shield below 200 km may be related to volcanism. The low-velocity feature near the eastern edge of the Arabian Shield and western edge of the Arabian Platform could be related to mantle flow effects near the interface of lithosphere of different thickness.

The results for crustal structure are consistent with previous studies, where applicable. New results for the lithosphere suggest that the mantle lithosphere is thin and the LVZ is significant near the Red Sea, where rifting is active. The mantle lid thickens away from the Red Sea in the Arabian interior. Furthermore, our results indicate the presence of polarization anisotropy in the lithospheric upper mantle, in the vicinity as well as farther away from the Red Sea. Our modeling suggests $v_{SV} > v_{SH}$ in the southern part of the Red Sea, consistent with vertical flow, and $v_{SH} > v_{SV}$ in the northern part of the Red Sea and the continental interior, as is commonly reported in the continents. The Moho appears to be gradational, but the crustal thickness does not exceed 40 km, which is consistent with the v_p/v_s analysis and inconsistent with a grid search analysis for receiver functions fits only. The mantle velocities are consistent with stable continental values.

Teleseismic shear-wave splitting along the Red Sea and across Saudi Arabia reveals that the stations in the Gulf of Aqabah display fast orientations that are aligned parallel to

Fig. 20 Topography, gravity signature, and lithospheric structure along cross-sectional profile AA'. **a** Topography along the profile plotted with a 32× vertical exaggeration (V.E.). The sediment thickness is shown by the grey shaded areas.

b Comparison of the observed gravity data from the GRACE satellites (*black dots*) and the calculated gravity (*grey line*) resulting from the structural model shown in **c**. The S-wave velocities (V_s) in km/s and densities (ρ) in g/cm^3 of each layer are listed (Hansen et al. 2007)

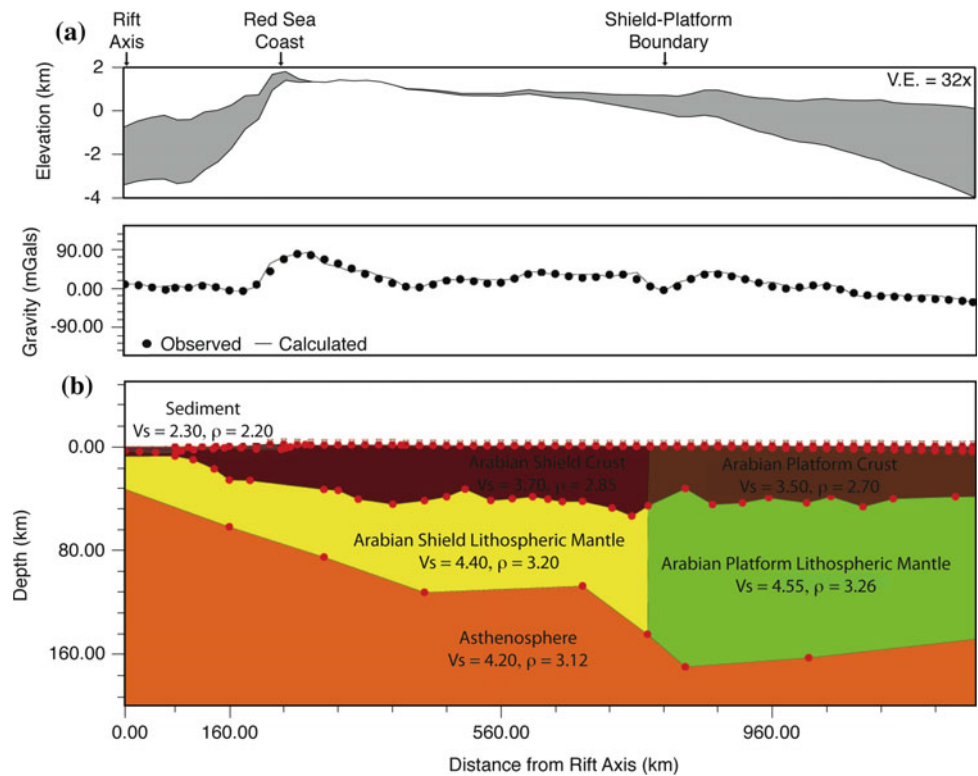


Table 1 Velocity model for the gulf of aqabah/dead sea region (V_P and V_S are the P- and S-wave velocities, respectively)

Depth (km)	Thickness (km)	V_P (km/s)	V_S (km/s)
0	2	4.50	2.60
2	5	5.50	3.18
7	10	6.10	3.52
17	11	6.20	3.60
28	∞	7.80	4.37

Table 2 Velocity model for the Arabian shield region

Depth (km)	Thickness (km)	v_p (km/s)	v_s (km/s)
0	1	4.0	2.31
1	15	6.20	3.58
16	20	6.80	3.93
36	∞	7.90	4.30

Table 3 velocity model for the arabian platform region

Depth (km)	Thickness (km)	v_p (km/s)	v_s (km/s)
0	4	4.00	2.31
4	16	6.20	3.64
20	20	6.4	3.70
40	∞	8.10	4.55

the Dead Sea Transform Fault. However, our observations across Saudi Arabia show a consistent pattern of north-south oriented fast directions with delay times averaging about 1.4 s. While fossilized anisotropy related to the Proterozoic assembly of the Arabian Shield may contribute to our

observations, we feel that the anisotropic signature is best explained by a combination of plate-motion and density driven flow in the asthenosphere. Shear caused by the absolute plate motion, which is directed approximately 40° east of north at about 22 mm/year, may affect the alignment

of mantle minerals. Combining the northeast oriented flow associated with absolute plate motion with the northwest oriented flow associated with the mantle plume beneath Afar generates a north-south oriented resultant that matches our splitting observations.

Acknowledgments The authors would like to express their thanks and gratitude to KACST (Project AR-23-40) and DSFP for funding this work. We would like also to extend our sincerest thanks to Drs. S. Hansen, A. Rodgers, A. Nyblade, H. Tkalic and Y. Park for their valuable support.

References

- Al-Amri AM (1995) Preliminary seismic hazard assessment of the southern Red Sea region. *J Europ earthq Eng* 3:33–38
- Al-Amri AM (1998a) The crustal structure of the western Arabian platform from the spectral analysis of long-period P-wave amplitude ratios. *Tectonophysics* 290:271–283
- Al-Amri AM (1998b) The crustal structure of the western Arabian platform from the spectral analysis of long-period P-wave amplitude ratios. *Tectonophysics* 290:271–283
- Al-Amri AM (1999a) The crustal and upper-mantle structure of the interior Arabian platform. *Geophys J Int* 136:421–430
- Al-Amri AM (1999b) The crustal and upper-mantle structure of the interior Arabian platform. *Geophys J Int* 136:421–430
- Al-Amri MS, Al-Amri AM (1999a) Configuration of the seismographic networks in Saudi Arabia. *Seism Res Lett* 70:322–331
- Al-Amri M, Al-Amri A (1999b) Configuration of the seismographic networks in Saudi Arabia. *Seism Res Lett* 70:322–331
- Al-Amri AM, Schult FR, Bufe CG (1991) Seismicity and aeromagnetic features of the Gulf of Aqabah (Elat) region. *J Geophys Res* 96:20179–20185
- Al-Amri AM, Mellors R, Vernon F (1999) Broadband seismic noise characteristics of the Arabian shield. *Arab J Sci Eng* 24(2A):99–113
- Al-Amri A, Rodgers A, Alkhalifah T (2004) Improving seismic hazard assessment in Saudi Arabia using earthquake location and magnitude calibration. In: *Proceedings of the third symposium on scientific research and technological development outlook in the Arab world*. Riyadh, Saudi Arabia
- Al-Damegh K, Sandvol E, Al-Lazki A, Barazangi M (2004) Regional seismic wave propagation (Lg and Sn) and Pn attenuation in the Arabian Plate and surrounding regions. *Geophys J Int* 157:775–795
- Al-Damegh K, Sandvol E, Barazangi M (2005) Crustal structure of the Arabian plate: new constraints from the analysis of teleseismic receiver functions. *Earth Planet Sci Lett* 231:177–196
- Ammon CJ (1991) The isolation of receiver effects from teleseismic P waveforms. *Bull Seism Soc Am* 81:2504–2510
- Badri M (1991) Crustal structure of central Saudi Arabia determined from seismic refraction profiling. *Tectonophysics* 185:357–374
- Ben-Menahem A (1979) Earthquake catalogue for the Middle East (92 BC–1980 AD). *Boll Geofisica Teor Appl* 21:245–310
- Benoit M, Nyblade A, VanDecar J, Gurrrola H (2003) Upper mantle P wave velocity structure and transition zone thickness beneath the Arabian shield. *Geophys Res Lett* 80. doi:10.1029/2002GL016436
- Bohannon RG, Naeser CW, Schmidt DL, Zimmerman RA (1989) The timing of uplift, and rifting peripheral to the Red Sea: a case for passive rifting? *J Geophys Res* 94:1683–1701
- Camp VE, Roobol MJ (1992) Upwelling asthenosphere beneath western Arabia and its regional implications. *J Geophys Res* 97:15255–15271
- Daradich A, Mitrovica J, Pysklywec R, Willett S, Forte A (2003) Mantle flow, dynamic topography, and rift-flank uplift of Arabia. *Geology* 31:901–904
- Debayle E, Lévêque JJ, Cara M (2001) Seismic evidence for a deeply rooted low-velocity anomaly in the upper mantle beneath the northeastern Afro/Arabian continent. *Earth Plan Sci Lett* 193:423–436
- Ebinger C, Sleep N (1998) Cenozoic magmatism throughout east Africa resulting from impact of a single plume. *Nature* 395:788–791
- El-Isa ZH (1990) Lithospheric structure of the Jordan-Dead Sea transform from earthquake data. *Tectonophysics* 180:29–36
- Evans JR, Achauer U (1993) Teleseismic velocity tomography using the ACH-method: theory and application to continental scale studies. *Seismic tomography: theory and practice*. Chapman and Hall, London, pp 319–360
- Gao S, Davis P, Liu H, Slack P, Rigor A, Zorin Y, Mordvinova V, Kozhevnikov V, Logatchev N (1997) SKS splitting beneath continental rift zones. *J Geophys Res* 102:22781–22797
- Gettings M, Blank H, Mooney W, Healey J (1986) Crustal structure of southwestern Saudi Arabia. *J Geophys Res* 91:6491–6512
- Hansen S, Schwartz S, Al-Amri A, Rodgers A (2006) Combined plate motion and density-driven flow in the asthenosphere beneath Saudi Arabia: Evidence from shear-wave splitting and seismic anisotropy. *Geology* 34(10):869–872
- Hansen S, Rodgers A, Schwartz S, Al-Amri A (2007) Imaging ruptured lithosphere beneath the Red Sea and Arabian Peninsula. Accepted for publication in *earth and planetary science letter*
- Jackson J, Fitch T (1981) Basement faulting and the focal depths of the larger earthquakes in the Zagros mountains (Iran). *Geophys J R Astron Soc* 64:561–586
- Julia J, Ammon CJ, Herrmann RB, Correig AM (2000) Joint inversion of receiver function and surface wave dispersion observations. *Geophys J Int* 143:99–112
- Julia J, Ammon CJ, Herrmann RB (2003) Lithospheric structure of the Arabian Shield from the joint inversion of receiver functions and surface-wave group velocities. *Tectonophysics* 371:1–21
- Karato SI (1998) Seismic anisotropy in the deep mantle, boundary layers and the geometry of mantle convection. *Pure Appl Geophys* 151:565–587
- Kennett B, Engdahl ER (1991) Travel times for global earthquake location and phase identification. *Geophys J Int* 105:429–465
- Langston CA (1979) Structure under mount rainier, Washington, inferred from teleseismic body waves. *J Geophys Res* 84:4749–4762
- Levin V, Park J (2000) Shear zones in the proterozoic lithosphere of the Arabian shield and the nature of the Hales discontinuity. *Tectonophysics* 323:131–148
- Levin V, Henza A, Park J, Rodgers A (2006) Texture of mantle lithosphere along the dead sea rift: recently imposed or inherited? *Phys Earth Planet Inter* (in press)
- Mechie J, Prodehl C, Koptschalitsch G (1986) Ray path interpretation of the crustal structure beneath Saudi Arabia. *Tectonophysics* 131:333–351
- Mellors RJ, Camp VE, Vernon FL, Al-Amri AMS, Gharib A (1999) Regional waveform propagation in the Arabian Peninsula. *J Geophys Res* 104:20221–20235
- Menke W, Levin V (2002) Anomalous seaward dip of the lithosphere-asthenosphere boundary beneath northeastern USA detected using differential-array measurements of Rayleigh waves. *Geophys J Int* 149:414–422
- Mokhtar T, Al-Saeed M (1994) Shear wave velocity structures of the Arabian Peninsula. *Tectonophysics* 230:105–125
- Mooney W, Gettings M, Blank H, Healy J (1985) Saudi Arabian seismic refraction profile: a travelttime interpretation of crustal and upper mantle structure. *Tectonophysics* 111:173–246

- Owens TJ, ZandL G, Taylor SR (1984) Seismic evidence for ancient rift beneath the Cumberland plateau, Tennessee: a detailed analysis of broadband teleseismic P waveforms. *J Geophys Res* 89:7783–7795
- Park Y, Nyblade A, Rodgers A, Al-Amri A (2005) Tomographic imaging of upper mantle P-and S-wave velocity heterogeneity beneath the arabian peninsula. UCRL-TR-214906
- Randall G (1994) Efficient calculation of complete differential seismograms for laterally homogeneous earth models. *Geophys J Int* 118:245–254
- Rodgers A, Schwartz SY (1998) Lithospheric structure of the Qiangtang Terrane, northern Tibetan Plateau, from complete waveform modeling: evidence for partial melt. *J Geophys Res* 103:7137–7152
- Rodgers A, Walter W, Mellors R, Al-Amri A, Zhang Y (1999) Lithospheric structure of the Arabian shield and platform from complete regional waveform modeling and surface wave group velocities. *Geophys J Int* 138:871–878
- Rodgers AJ, Harris D, Ruppert S, Lewis JP, O’Boyle J, Pasyanos M, Fandi Abdallah AQ, Al-Yazjeen T, Al-Gazo A (2003) A broadband seismic deployment in Jordan. *Seism Res Lett* 74:374–381
- Rodgers A, Tkalcic A, Nyblade A, Park A, Schwartz S, Hansen S (2005) Upper mantle structure beneath the Arabian Shield and Red Sea. Unpublished report, LLNL
- Sandvol E, Ni J, Ozalaybey S, Schlue J (1992) Shear-wave splitting in the rio grande rift. *Geophys Res Lett* 19:2337–2340
- Sandvol E, Seber D, Barazangi M, Vernon F, Mellors R, Al-Amri A (1998a) Lithospheric seismic velocity discontinuities beneath the Arabian shield. *Geophys Res Lett* 25:2873–2876
- Sandvol E, Seber D, Calvert A, Barazangi M (1998b) Grid search modeling of receiver functions: implications for crustal structure in the Middle East and North Africa. *J Geophys Res* 103:26899–26917
- Savage MK, Silver PG, Meyer RP (1990) Observations of teleseismic shear wave splitting in the Basin and range from portable and permanent stations. *Geophys Res Lett* 17:21–24
- Schilling J, Kingsley R, Hanan B, McCully B (1992) Nd-Sr-Pb isotopic variations along the Gulf of Aden: evidence for Afar mantle plume—continental lithosphere interaction. *J Geophys Res* 97:10927–10966
- Schmid C, van der Lee S, Giardini D (2004) Delay times and shear wave splitting in the Mediterranean region. *Geophys J Int* 159:275–290
- Schmidt DL, Hadley DG, Stoeser DB (1979) Late Proterozoic crustal history of the Arabian Shield, southern NaJd province, Kingdom of Saudi Arabia, evolution and mineralization of the Arabian-Nubian Shield. *IAG Bull* 3:41–58
- Schwartz SY, Rodgers A, Russell S (2000) Crustal and upper mantle structure beneath northeast Africa and the Red Sea Rift Zone. In: Ryerson FJ, Cook KH, Tweed J (eds) Institute of geophysics and planetary physics, annual report. Lawrence Livermore National Laboratory
- Seber D, Mitchell B (1992) Attenuation of surface waves across the Arabian Peninsula. *Tectonophysics* 204:137–150
- Seber D, Vallve M, Sandvol E, Steer D, Barazangi M (1997) Middle east tectonics: applications of geographical information systems (GIS). *GSA Today* 1–5
- Silver P, Holt W (2002) The mantle flow field beneath Western North America. *Science* 295:1054–1057
- Sodoudi F (2005) Lithospheric structure of the Aegean obtained from P and S receiver functions. Ph.D. Thesis, Freie Universitat Berlin
- Stoeser D, Camp V (1985) Pan-African microplate accretion of the Arabian shield. *Geol Soc Am Bull* 96:817–826
- Thurber CH (1983) Earthquake locations and three-dimensional crustal structure in the Coyote Lake area, central California. *J Geophys Res* 88:8226–8236
- Tkalcic H, Pasyanos M, Rodgers A, Gok R, Walter W, Al-Amri A (2005) A multi-step approach in joint modeling of surface wave dispersion and teleseismic receiver functions: Implications for lithospheric structure of the Arabian Peninsula, UCRL-TR-214906
- VanDecar JC (1991) Upper mantle structure of the Cascadia subduction zone from non-linear teleseismic travel time inversion, Ph.D. thesis, Univ. of Wash., Seattle
- VanDecar JC, Crossen RS (1990) Determination of teleseismic relative phase arrival times using multi-channel cross-correlation and least-squares. *Bull Seismol Soc Am* 80:150–161
- Vernon F, Berger J (1997) Broadband seismic characterization of the Arabian Shield, Final Scientific Technical Report, Department of Energy Contract No. F 19628-95-K-0015, 36 pp
- Vernon F, Mellors R, Berger J, Edelman A, Al-Amri A, Zollweg J, Wolfe C (1996) Observations from regional and teleseismic earthquakes recorded by a deployment of broadband seismometers in the Saudi Arabian shield. *EOS Trans AGU* 77(46):478
- Wolfe CJ, Vernon FL, Al-Amri A (1999) Shear-wave splitting across western Saudi Arabia: The pattern of mantle anisotropy at a Proterozoic shield. *Geophys Res Lett* 26:779–782